JOURNAL OF GEOPHYSICAL RESEARCH, VOL. 102, NO. B6, PAGES 12,295–12,315, JUNE 10, 1997

Thermal and dynamical evolution of the upper mantle in subduction zones

Chris Kincaid
Graduate School of Oceanography, University of Rhode Island, Narragansett

I. Selwyn Sacks
Department of Terrestrial Magnetism, Carnegie Institution of Washington, Washington, D.C.

Abstract. We present results from two-dimensional (2-D) numerical experiments on the thermal and dynamical evolution of the subducting slab and of the overlying mantle wedge for a range in subduction parameters. These include subduction rate and the age and rheology of both subducting and overriding plates. Experiments also consider the influence of slab forcing conditions (from purely kinematic to purely dynamic) on the evolution of both the slab and mantle wedge. One goal is to determine how different parameters control thermal evolution of the slab-wedge interface, from just after subduction initiation up through roughly 500-600 km of subduction, where temperatures are approaching steady state. An additional goal is to define optimal conditions for the melting of slab sediments and crust. Results show slab surface temperatures (SSTs) depend strongly on subduction velocity, plate thermal structure, and upper mantle (or wedge) viscosity structure. Fast subduction beneath a thick (>70 km) overriding plate results in the coolest SSTs. Maximum SSTs are recorded as an early transient event for cases of slow subduction (<3 cm/yr) beneath young, thin lithosphere (<45 km). The latter result supports a model for melting of slab sediments, and possibly crust, early on in cases where young plates subduct beneath thin lithosphere, such as in the Cascades. Maximum wedge temperatures are recorded at higher subduction rates and are found to be strongly dependent on factors influencing return flow into the wedge, such as age of the overriding plate and the ratio of retrograde to longitudinal slab motion. Assuming a model for arc magma genesis driven by fluids migrating into the wedge, these results predict higher-temperature, Mg-rich melts coming up beneath subduction zones with fast, steep slabs and young overriding plates, such as in Japan. The influence of variable viscosity is most pronounced in the slab-wedge corner, which tends to stagnate, or freeze out, with time. Moreover, a region of highly viscous mantle develops above the slab at intermediate depths (>100 km) which deflects the zone of maximum shear away from slab-wedge interface.

Introduction

A number of relevant geophysical problems involve subduction. On a large scale, subducting plates provide a dominant driving force in mantle convection and the tectonics of surface plates. Moreover, the subduction of oceanic lithosphere to depths of at least 670 km strongly influences both the thermal and chemical evolution of the mantle. On a smaller scale, the current 40,000 km of subduction zones represent important sites of thermal and chemical exchange between the deep Earth and Earth's surface. While it is clear that exchange processes at convergent margins are driven by subduction, questions regarding how oceanic sediments and crust are recycled through the arc system and what factors control slab-wedge thermal evolution and subsequent magmagenesis and transport in arcs remain unresolved.

Geophysical observations are providing increasingly detailed snapshots of subduction morphology. Seismic studies provide an instantaneous view of subduction, including slab and wedge temperature structure [*Zhao and Hasegawa*, 1993; *Van der Hilst et al.*, 1991, 1993; *Ohtaki and Kaneshima*, 1994; *Abers*, 1994]. More specifically, seismic body wave [*Helffrich and Stein*, 1993; *Matsuzawa et al.*, 1987] and tomographic studies [*Zhao and Hasegawa*, 1993; *Van der Hilst* et al., 1991, 1993] are providing clearer images of mantle wedge-slab seismic velocity structure and potential low-density magma source regions. A low-velocity region above the Japan slab [*Matsuzawa et al.*, 1986, 1987] has been suggested to be the hydrated peridotite discussed in *Tatsumi's* [1989] model for arc magmagenesis. Tomography results beneath Japan [*Zhao and Hasegawa*, 1993] also indicate a low-velocity (presumably hot) tongue intruding into the wedge, just above the slab, which might indicate a warmer return flow into the wedge. While the low- velocity region does not connect with the slab surface, an alternative interpretation of these patches of slow mantle is that they also represent hydrated regions of the mantle wedge.

An additional morphological feature of subduction is suggested by variability in seismic attenuation from the trench side of the volcanic front to the back arc side of the front [*Sacks*, 1975; *Umino and Hasegawa*, 1984]. Specifically, results from a study of subduction beneath Japan show an inferred viscosity structure within the wedge which includes a nearly vertical front between low Q (100)-low-viscosity region beneath the volcanic front and an inner high Q (300)-high-viscosity region occupying the arc corner. This type of lateral structure oriented about the volcanic front is consistent with

Copyright 1997 by the American Geophysical Union.

Paper number 96JB03553.
0148-0227/97/96JB-03553$09.00

heat flow data across arcs, such as the northern margin of the Cascades [*Hyndman*, 1988], which typically shows enhanced heat flow (≈ 2 HFU or ≈ 80 mW/m^2) on the back arc side of the front rank of arc volcanoes and reduced values on the trenchward side of the arc (<1 HFU). Heat flow data across Japan show this type of trend [*Furukawa and Uyeda*, 1989] and have been used, in conjunction with simple thermal models, to argue for cool slab surface temperatures at shallow subduction levels (<200°C) and for negligible frictional heating at the slab surface.

An interpretation which reconciles heat flow observations with estimates of seismic Q is that temperatures trenchward of the front, within this apex region of the mantle wedge are very low [*Sato and Sacks*, 1990]. However, Q values behind the front are sufficiently high to indicate this material is not beyond its dry solidus. If it is accepted that the laboratory measurements of *Sato and Sacks* [1990] made sufficient allowance for frequency dependence of attenuation [e.g., *Jackson et al.*, 1992], then the mantle wedge is essentially below its dry solidus temperature, though well above the wet solidus.

In addition to seismicity and other geophysical data sets, chemical transport associated with fluid migration and magmatism is both a response to, and useful probe of, subduction-driven processes. The ability to track distinct slab-derived chemical constituents through the trench-mantle wedge-arc system constrains the temporal evolution of arcs and, when combined with seismic data and dynamic modeling, provides strong limits on the range of acceptable models for arc magma generation and transport [e.g., *Davies and Bickle*, 1991]. Chemical data sets provide direct evidence for slab involvement in arc recycling and crustal growth processes and constrain magma ascent times. One important tracer has been ^{10}Be [*Morris et al.*, 1990], which is produced cosmogenically and attaches to particles which settle out in sediments draping the ocean floor. Detection of ^{10}Be in arc magmas provides direct evidence for sediment subduction to the depths of arc magmagenesis and is clear evidence for a slab-derived component in arc magmas. Moreover, the 1.5 Ma half-life of ^{10}Be demands that generation and transport of magma be rapid. U-Th data [*Reagan et al.*, 1994] suggest even shorter ascent times for magma, perhaps as low as 10^5-10^6 years, which is evidence against stokes spheres (or plumes) as the primary mode of magma transport.

The combination of boron (B) and ^{10}Be data sets further constrain arc processes [*Edwards et al.*, 1993; *Gill et al.*, 1993; *Morris et al.*, 1990]. For example, *Morris et al.* [1990] show that a B/^{9}Be mixing line spans a range from an enriched source to pristine (with respect to B) background. Since B does not decay, this is strong evidence that the magma moves through the wedge independent from the matrix and without contaminating the wedge in the process. B-Be systematics have been used to support models in which the mantle wedge melts in response to a flux of slab-derived fluids [*Edwards et al.*, 1993; *Gill et al.*, 1993; *Morris et al.*, 1990], rather than melting of the slab itself [*Marsh*, 1979; *Hsui et al.*, 1983]. However, there does appear to be evidence for melting of the uppermost slab (crustal component) associated with subduction of young lithosphere during the early stages of subduction [*Drummond and Defant*, 1990].

Through a combination of geochemical and geophysical data and results from dynamical process models of melt production and transport [*Davies and Bickle*, 1991; *Davies and Stevenson*, 1992; *Spiegelman and McKenzie*, 1987], a clearer picture of arc systematics is emerging. However, magma generation and transport models ultimately rely on thermal and dynamical conditions within the upper mantle in subduction zones. Here we develop a dynamical model of subduction to determine what factors are most important in influencing slab thermal evolution and conditions within the wedge where magmas ultimately take source. The 2-D Cartesian model of subduction considers flow in the wedge resulting from the sinking slab, as well as flow due to local buoyancy forces within the wedge. A salient feature of the model is that the slab in these experiments is defined chemically, using tracer particles which are tracked with the circulation. In this way the upper surface of the slab moves freely through the model domain and is not necessarily a prescribed velocity boundary condition. Initial experiments focus on defining subduction conditions which give rise to slab surface temperatures (SSTs) sufficient to trigger melting of sediments. One model of arc magmagenesis suggests slab-derived fluids migrating into the wedge trigger melting when temperatures exceed the wet solidus. Therefore experiments also track P-T conditions within the wedge for a range in subduction parameters. Results show maximum SSTs occur with slow subduction beneath thin plates. Maximum wedge temperatures are recorded when a fast plate subducts beneath a young overriding plate and in cases where slabs sink with higher ratios of retrograde to longitudinal motion (e.g., Figure 3b). In general, thicker overriding plates and shallower dip angles restrict return flow into the wedge resulting in cooler slab and wedge temperatures.

Previous Work on Subduction Dynamics

Problems related to subduction extend from the shallow dynamics of the trench and accreationary wedge to larger-scale processes, such as the fate of slabs at 670 km [*Christensen and Yuen*, 1984; *Gurnis and Hager*, 1988; *Tao and O'Connell*, 1992; *Zhong and Gurnis*, 1994] and within the lower mantle [e.g., *Christensen*, 1989; *Olson and Kincaid*, 1991]. Numerical models have been applied to questions regarding the larger-scale coupling between subducted slabs, mantle flow, and back arc spreading including corner flow models [*Toksoz and Bird*, 1977; *Tovish et al.*, 1978] and models with flow driven by applied global plate motions [*Harper*, 1978; *Hager and O'Connell*, 1978; *Chase*, 1978; *Parmentier and Oliver*, 1979]. Models have also considered effects of retrograde slab-trench motion [*Garfunkel et al.*, 1986; *Tao and O'Connell*, 1992; *Kincaid and Olson*, 1987; *Shemenda*, 1992, 1993] and effects of throughgoing faults at the trench [*Zhong and Gurnis*, 1992].

A number of studies have used kinematic models of subduction, coupled with thermal modeling, to estimate the shallow thermal evolution of subducting lithosphere, specifically the role of shear heating in compressional environments [*Molnar et al.*, 1983; *Barr and Dahlen*, 1989; *Molnar and England*, 1990]. One study shows that in addition to increased frictional heating levels, decreasing subduction angle, decreasing subduction rate, and increasing presubduction geothermal gradient all lead to increased forearc temperatures [*Dumitru*, 1991]. Similar kinematic studies have followed slab thermal evolution deeper into the system, almost to the point where the slab surface emerges from beneath the overriding plate into the more fluid upper mantle [*Peacock*, 1991, 1992; *Peacock et al.*, 1994] and been used to argue against significant shear heating at shallow levels.

The focus of this work is on subduction at intermediate depth levels, or from when the slab enters the mantle down to the base of the upper mantle, and questions of how the slab and wedge evolve thermally and dynamically. Such intermediate-scale slab models provide the physical context for more complex chemical transport models in arcs which attempt to describe how and where magma is produced and how it ascends through, and interacts with, the upper mantle. Three distinct conceptual/theoretical models of magma generation and transport are as follows: (1) magmas are produced from melting of the slab sediments and crust and rise as gravitational instabilities [*Marsh*, 1979], (2) hydrous fluids released from the slab permeate the mantle wedge and trigger melting and subsequent diapiric or crack instabilities in the wedge [*Davies and Stevenson*, 1992] and (3) melt generated in the wedge by release of hydrous phases migrates as a porous flow, through interconnected channels in the mantle matrix [*Spiegelman and McKenzie*, 1987].

Two distinct modes of flow are represented in these models including the sluggish flow of the mantle matrix and the porous flow of melt relative to the mantle matrix [*Spiegelman and McKenzie*, 1987]. Moreover, two types of large-scale convection of the matrix may be defined. From the perspective of the wedge, the sinking slab drives a forced, corner flow circulation in the mantle wedge [e.g., *Toksoz and Bird*, 1977; *Tovish et al.*, 1978]. Free convection in the wedge, such as in the form of low-density diapirs, would be driven by chemical and/or thermal density anomalies arising from the volatile input from the slab. Previous work on matrix flow at these intermediate scales in subduction zones includes conductive thermal models of the slab [e.g., *Toksoz et al.*, 1971; *Anderson et al.*, 1978] and coupled thermal and kinematic flow models [*Hsui et al.*, 1983; *Staudigel and King*, 1992; *Davies and Stevenson*, 1992; *Furukawa*, 1993a, b; *Peacock et al.*, 1994]. In these cases, slab motion is prescribed, or forced. Ideally, a physical model of magma processes in subduction zones should include the thermal-chemical evolution of the slab-mantle wedge system and both the free and forced convective aspects of subduction. A limited number of model studies have considered P-T paths of freely sinking slabs [*King and Ita*, 1995] and, more specifically, free convection within the mantle wedge [*Marsh*, 1979; *Jurdy and Stefanick*, 1983; *Richards and Davies*, 1989; *Sacks and Kincaid*, 1990; *Davies and Stevenson*, 1992; *Kincaid et al.*, 1994].

Model

We develop a model of slab-mantle dynamics to focus on thermal and dynamical evolution of the upper mantle in subduction zones which will provide the context for models of magma generation and the coupled flow of both melt and matrix [*Spiegelman et al.*, 1994]. An important feature of the model is that the slab is not a fixed, kinematic boundary but can deform and freely evolve within the fluid domain. One goal is to determine the relative importance of various subduction parameters in modulating slab-wedge evolution, including subduction rate and both thermal and rheological structure of the overriding and subducting plates. Experiments also consider how different modes of slab forcing, from purely kinematic to purely buoyant slabs, produce different subduction morphologies (e.g., levels of retrograde slab motion) and how these differences influence the thermal evolution of both slab and mantle wedge. At one extreme are cases where slabs are pushed or driven (e.g., ridge push) without any buoyancy forces. An alternative mode of forcing is one where a slab sinks due to anomalous density (e.g., slab pull forces). A number of "mixed" cases are presented in which subduction results from a combination of an applied velocity and internal buoyancy forces. This mixed mode of forcing is optimal for investigating slab-wedge evolution for various plate rates/ages given a fixed slab dip angle. These cases then provide a reference against which conditions in experiments with various subduction morphologies (driven versus buoyant, or retrograde versus prograde) may be compared. In all experiments presented here, flow within the wedge evolves freely, although it is primarily dominated by the motion of the slab, regardless of the mode of slab forcing.

Numerical experiments model convection of a viscous, Boussinesq, Newtonian fluid within a two-dimensional (2-D) Cartesian geometry. The system of dimensionless model equations include conservation of (1) mass, (2) momentum, and (3) energy which are written in vector notation as

$$\nabla \cdot \mathbf{u} = 0 \tag{1}$$

$$\nabla \cdot \tau + \nabla p = \mathrm{Ra}\, T \hat{k} + B\, \mathrm{Ra}\, C \hat{k} \tag{2}$$

$$\partial T/\partial t = -\mathbf{u} \cdot \nabla T + \nabla^2 T\,. \tag{3}$$

Dimensionless variables $\mathbf{u}$, τ, p, C, and T are the velocity vector, the viscous stress tensor, pressure, composition, and temperature, respectively. Here $\hat{k}$ is the unit vector in the vertical direction. The parameters controlling strength of buoyantly driven flow in the body force term in (2) are the thermal Rayleigh number

$$\mathrm{Ra} = g\alpha \Delta T D^3 / \kappa\eta, \tag{4}$$

and a dimensionless buoyancy parameter

$$B = \Delta\rho_c/\rho\ \alpha\ \Delta T, \tag{5}$$

relating the density contrast due to compositional variations in the fluid to those due to thermal variations. Here ΔT is the total vertical potential temperature difference (degrees Celcius) across the box. Parameters g, κ, α, D, and η are gravity, thermal diffusivity, thermal expansion coefficient, fluid thickness, and kinematic viscosity, respectively.

In this formulation, fluid motion may be driven by both thermal and compositional fields. Slab fluid is tagged compositionally within this model to facilitate tracking SSTs over a range in subduction morphologies and to provide flexibility in assigning specific physical characteristics to the model slabs, as discussed in more detail below. Because the body force in (2) is a function of C, the system of model equations must include a conservation equation for chemical species. A nondiffusive, Lagrangian particle technique is employed for tracking fluid chemistries [e.g., *Christensen*, 1992; *Kincaid et al.*, 1996], whereby individual particles are transported with the flow by solving the simple advection equations

$$\frac{d\mathbf{x}}{dt} = \mathbf{u}, \tag{6}$$

using a Runge-Kutta step. Here $\mathbf{x}$ is a position vector. Slab concentration is then calculated from

$$C_k = P_k / P_o, \tag{7}$$

where P_k and P_o are the number of particles within cell k and the initial maximum number of particles per cell within the slab. C varies between 0 and 1 for ambient upper mantle and slab chemistries, respectively. Approximately 100,000 tracer

Table 1a. Parameters for Numerical Experiments for Mixed Cases

Case	Pe	E	Ra_δ OP	Ra_δ SP	B	Dip Angles, deg	R_θ	Depth of Weak Nodes, km	Grid	Max SST at 160 km
					Pe Variation					
1	100	30	500	500	0	45-55	0-0.175	130	F	
2	400	30	500	500	0	45-55	0-0.175	130	F	
3	800	30	500	500	0	45-55	0-0.175	130	F	
4	2000	30	500	500	0	45-55	0-0.175	130	F	
5	3000	30	500	500	0	45-55	0-0.175	130	F	
6	5000	30	500	500	0	45-55	0-0.175	130	F	
7	100	30	75	75	1.25	45	0	130	F	
8	400	30	75	75	1	45	0	130	F	
9	800	30	75	75	.625	45	0	130	F	
10	1500	30	75	75	0	45	0	130	F	
11	2000	30	75	75	0	45	0	130	F	
12	2500	30	75	75	0	45	0	130	F	
13	3000	30	75	75	0	45	0	130	F	
14	5000	30	75	75	0	45	0	130	F	
2-C	400	30	500	500	0	45	0	130	C	0.67(0.72)
11-C	2000	30	75	75	0	45-55	0-0.175	130	C	0.48(0.5) 0.265(0.29)[a]
					Variable E[b]					
15	3000	8	500	500	0	60-70	0.25-0.45	130	F	0.52
16	3000	15	200	200	0	50-60	0.1-0.25	130	F	0.49
13	3000	30	75	75	0	45	0	130	F	0.46
17	300	15	500	500	0	50-60	0.1-0.25	130	C	0.66
18	3000	15	500	500	0	50-60	0.1-0.25	130	C	0.52
19	300	15	75	75	0	45-50	0-0.1	130	C	0.54
20	3000	15	75	75	0	45-50	0-0.1	130	C	0.44
					Variable Plate Age[c]					
21	400	30	500	75	0	45-60	0-0.25	130	F	
22	400	30	75	500	0	45-50	0-0.1	130	F	
23	3000	30	500	75	0	45-60	0.25	130	F	
24	3000	30	75	500	0	45-50	0-0.1	130	F	
					Variable R_θ[d]					
25	2000	30	75	75	-1.25	<40	-(0.1-0.5)	130	F	0.5 (0.76)
26	2000	30	75	75	.3	45-50	0-0.1	130	F	0.5 (0.89)
27	2000	30	75	75	1.25	45-70	0-0.45	130	F	0.5 (0.92)
28	2000	30	75	75	3.75	45-90	0-1	130	F	0.5 (0.985)
					Reduced Depth Extent of Weak Nodes					
29	400	30	75	75	0	<40	-(0.1-0.5)	110	F	
30	400	30	75	75	2.5	45	0	110	F	
31	400	30	75	75	7.5	45-80	0-0.7	110	F	
32	400	30	75	75	12.5	45-90	0-1	110	F	
33	2000	30	75	75	0	<40	-(0.1-0.5)	110	F	
34	2000	30	75	75	1.25	<40	-(0.1-0.5)	110	F	
35	2000	30	75	75	7.5	<40	-(0.1-0.5)	110	F	
36	2000	30	75	75	12.5	45	0	110	F	
37	400	30	75	75	0	<40	-(0.1-0.5)	90	F	
38	400	30	75	75	7.5	45	0	90	F	
39	400	30	75	75	12.5	45-80	0-0.7	90	F	

$R_\theta = 0$; slabs driven at given Pe and Ra = 800,000. In some cases, B is set $\neq 0$ to maintain 45° dip. Maximum SST information is provided for specific cases.

[a]Maximum SST at 70 km.

[b]Cases 15, 16, and 13 are compared in Plate 2.

[c]Subducting versus overriding plates.

[d]Maximum wedge temperature along vertical line from slab at 160 km.

Table 1b. Parameters for Numerical Experiments for Variable Modes of Forcing

Case	Pe	E	Ra_δ OP	Ra_δ SP	B	Dip Angles, deg	R_θ	Depth of Weak Nodes, km	Grid	Measured Slab Pe
					Pure Driven[a]					
40	3000	30	200	200	0	<40	-(0.1-0.5)	110	F	
					Pure Buoyancy[b, c]					
41		30	75	75	1	45-80	0-0.7	110	F	220
42		30	75	75	2	45-80	0-0.7	110	F	500
43		30	75	75	4	45-80	0-1	110	F	1000
44		30	75	75	5.5	45-80	0-1	110	F	1650

[a]Ra = 0.
[b]No applied Pe; free slip on upper boundary.
[c]Maximum SST is not applicable to these calculations because they begin with fields from case 13 just after the slab tip has pierced the 160 km depth horizon. However, for comparison late stage SSTs are .37 (160 km) and .26 (70 km) versus .25 (160 km) and .07 (70 km) for mixed, R_θ=0, cases with similar subduction rate and plate characteristics.

particles are used to represent chemically distinct slab material within these experiments with initial particle concentrations in excess of 100 per cell. The number of particles per cell was selected after running numerical experiments, with similar forcing parameters, for a range in particle densities (10,000-400,000) to establish the sensitivity of the solution to total particles.

The dominant viscosity gradient modeled here is between the lithosphere and the ambient (or deep) mantle. A highly viscous lithosphere is produced through an exponential relationship between viscosity (μ) and temperature written

$$\mu(T,C) = \mu_o(C) \exp [E ((1/T) - 1)] . \qquad (8)$$

The parameter μ_o is the reference viscosity, which can vary with C as discussed below, and E is directly related to activation energy, ε, and inversely related to ΔT and the gas constant, R. The magnitude of E modulates the rheological boundary layer thickness for a given thermal profile (Figure 2b). The range in values considered here are given in Table 1. A maximum, or cutoff, thermal viscosity is assigned a dimensionless value of 1000.

Plate-Like Subduction

In these experiments we seek to match as closely as possible a few basic, observed characteristics of subduction and subduction morphology. One important characteristic is that slabs sink as tabular, plate-like features within the upper mantle covering a range in dip angles and subduction rates. A limitation of subduction modeling, however, is an inherent difficulty in representing the physics of the trench in such a way as to allow for plate-like subduction. In a strongly temperature dependent viscous fluid, cool temperatures associated with the upper thermal boundary layer tend to produce a stagnant lid, rather than a subducting plate [*Jacoby and Schmeling*, 1982; *Ogawa et al.*,1991]. A more realistic pattern of subduction has been produced by using weak nodes to represent the trench [*Davies*, 1986; *Schmeling and Jacoby*, 1981; *Gurnis and Hager*, 1988] or a strongly power law rheology [*King and Hager*, 1990; *Schmeling*, 1989; *van den Berg et al.*, 1991]. *King and Hager* [1990] compare the two techniques and show that both produce reasonable strain rates but that subduction velocities are generally larger with weak nodes.

Plate-like subduction is produced in two ways in these experiments. First, weak nodes are incorporated into the model by assigning a reduced, μ=0.01, viscosity within a fixed region of the domain (Figures 1 and 2c). This region is two elements wide and extends from the trench down into the mantle at a 45° dip angle (maximum depth of weak nodes are listed in Table 1). Starting from the base of the overriding plate, weak node viscosity is ramped to ambient viscosity conditions (μ=1 at T=1 and C=0) at the base of weak node region. In addition, we take advantage of our ability to define the slab fluid compositionally by modeling a moderate viscosity increase within the subducting plate, relative to the overriding plate. This technique is employed as an additional means of insuring a tabular, plate-like subduction morphology. The compositional viscosity variation is modeled by allowing μ_o in (8) to vary with concentration through the expression

$$\mu_o(C) = 1 + [(\mu_s-1)/2] [1+\tanh(\gamma (C-0.25))], \qquad (9)$$

where μ_s is dimensionless slab (C=1) viscosity at a reference (T=1) dimensionless temperature and γ is a constant controlling the form of the viscosity function moving between slab and upper mantle material. Figure 2a shows a graphical representation of the functional dependence of μ_o on slab concentration. This law for preexponential viscosity, along with values for the transition composition of C=0.25 and γ=10, were chosen through a series of preliminary experiments to insure a sharp transition in material properties between the slab and ambient mantle.

Approximately 50 preliminary experiments were run in order to map out subduction morphologies for a wide range in weak node formulations and parameters controlling slab compositional viscosity changes described in (9). Cases included a variety of weak node viscosity magnitudes, from 10^{-3} to 10, and different scenarios for tapering weak nodes both laterally, into the overriding plate, and vertically, through the plate and into the upper mantle. In a number of these experiments, particularly those with more complicated lateral weak node tapering schemes, the requirement of plate-like morphology was compromised. Slabs tended to be either severely underplated beneath the overriding plate if weak nodes were terminated at too shallow a level or to become bound up in the trench leading to a form of subduction dominated by a single boundary layer instability. A relatively simple

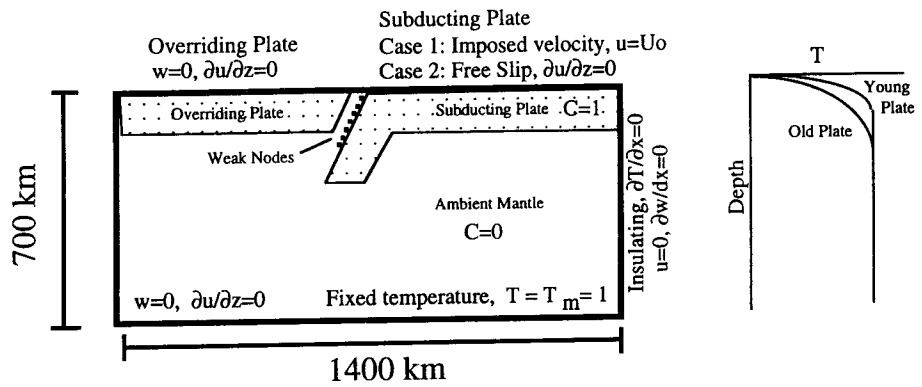

Figure 1. Schematic showing model geometry and boundary conditions. Here T_m is ambient (deep) upper mantle potential temperature. Bottom and sides are insulating and free slip. A distinction is made between subducting (SP) and overriding plates (OP), and the positions of the weak nodes and trench are shown. Also shown are schematic examples of young (45 km) versus old (70 km) plates as defined by their initial thermal profile.

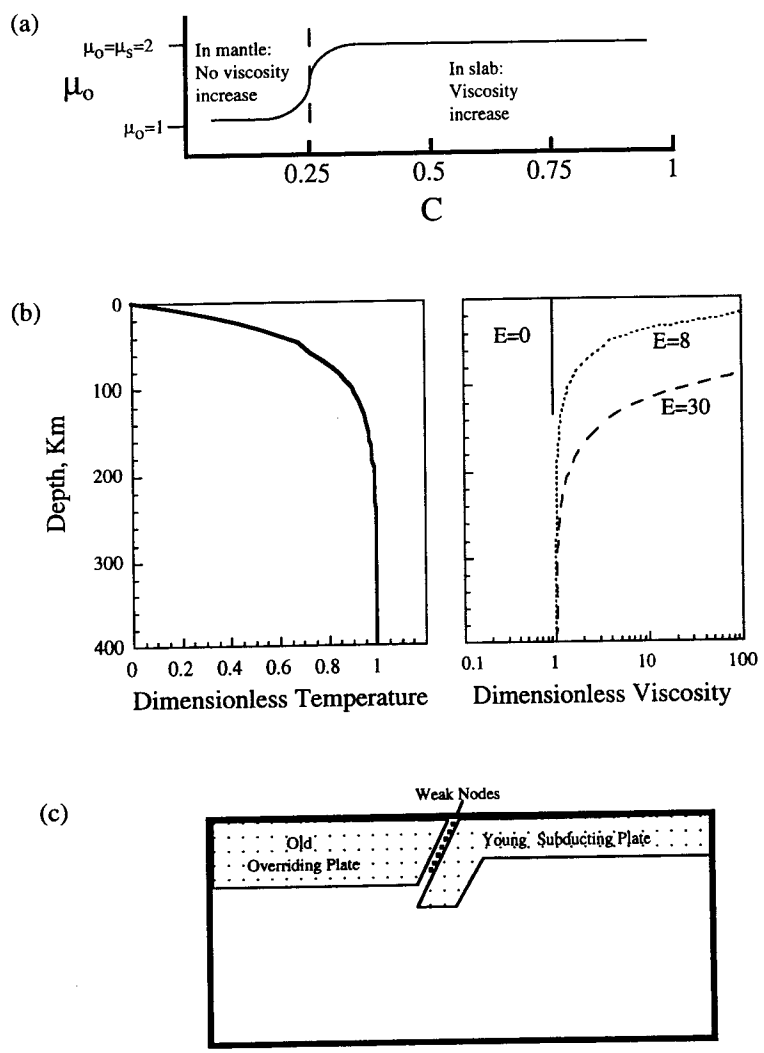

Figure 2. (a) Plot of preexponential viscosity coefficient versus slab concentration (as described in (9)). (b) Plots of T and μ versus depth showing relative thermal and viscosity boundary layer thicknesses for various dimensionless activation energies (E). For a given thermal profile, a larger E produces a thicker viscosity boundary layer. (c) Schematic illustrating how subducting plates (SP) and overriding plates (OP) may be modeled with different plate ages/thicknesses through (12).

formulation involving a fixed pattern of weak nodes described above, coupled with a modest increase in isothermal viscosity of the subducting (C=1) plate was found to consistently produce plate-like subduction morphology. A value of $[\mu_o(C=1)/\mu_o(C=0)] = 2$, used in all cases reported here, was found to successfully limit the adherence and binding of slab material to the overriding plate for the chosen weak node formulation.

Model Domain and Boundary Conditions

The 2-D domain represents a slice of the upper mantle oriented vertically and aligned perpendicular to the trench. Figure 1 shows the basic model setup and a sample initial plate configuration. The horizontal and vertical dimensions of the 2-D box are 1400 km and 700 km (Figure 1). Experiments are conducted using a coarse (96 elements in the horizontal direction and 48 elements in the vertical direction) and a fine (192x96) scale uniform grid. Examples of experiments with each grid are given in Table 1, although each of the fine grid cases listed here have also been run with the coarse grid. One primary difference in results between grids is that slab surface temperatures on the course grid are generally 7-8% lower than their fine grid counterparts given similar subduction parameters and subduction morphologies.

The bottom and sidewalls of the model domain are impermeable, free slip boundaries. Upper and lower boundaries are assigned constant values of temperature and zero temperature gradient conditions apply on the sidewalls. The upper boundary is impermeable and the condition on horizontal velocity varies depending on whether you are in the overriding or subducting plates (Figure 1). The overriding plate is represented with a free slip, or $\partial u/\partial z=0$, upper boundary condition. Subducting plates are modeled using one of two possible modes. In cases where there is a driven, or kinematic, component of slab motion (experiments 1-40 in Table 1), the region to the right of the trench in Figure 1 is assigned a prescribed pattern in horizontal velocity U_o. Velocity is zero at the upper right corner and ramps up over three grid points to the applied value (U_o) which is uniform over the subducting plate. At the trench, the subduction rate U_o is applied as a velocity vector dipping at 45°. For an additional class of experiments, in which slabs are solely driven by buoyancy forces (cases 41-44 in Table 1), the boundary condition above the subducting slab is free slip, which is similar to that imposed above the overriding plate.

The system of model equations is solved subject to these boundary conditions and initial conditions on both thermal and compositional fields using a penalty function, finite element technique which utilizes bilinear splines. The solution procedure for mass, momentum and energy is described in more detail elsewhere [*Brooks*, 1981; *Hughes*, 1987; *King et al.*, 1990; *Kincaid*, 1990] and has been benchmarked [*Travis et al.*, 1991]. The initial compositional field is an 80 km thick by roughly 700 km wide patch of lithosphere to the right of the trench which is assigned a value of C=1 (Figure 1). Initial thermal, and therefore rheological, fields are calculated using the expression

$$T(x,z')=1-\exp(-z'/\delta(x)) , \qquad (10)$$

where δ is a dimensionless boundary layer thickness parameter used in defining a boundary layer Rayleigh number (Ra_δ) and z' is depth.

An important model feature is that it is possible to distinguish between overriding and subducting plates in terms of temperature, such as young versus old plate ages depicted in Figures 1 and 2c. For modeling cases in which an old plate subducts beneath a young plate, as in Japan, or the alternative case, δ is made to be a function of horizontal position, x, through the dimensionless expression

$$\delta(x) = 3 / [Ra_\delta(x)]^{1/3}. \qquad (11)$$

Here Ra_δ varies in the horizontal direction about a fixed trench position (x_T) using a hyperbolic tangent function (e.g., a similar functional form to that shown in Figure 2a) written as

$$Ra_\delta(x) = Ra_\delta^R + [(Ra_\delta^R - Ra_\delta^L) / 2] \, [1+\tanh(\gamma_\delta (x-x_T))]. \qquad (12)$$

Here superscripts L and R represent values for the left and right sides of the trench and γ_δ is a constant similar to γ in (9) that is also set to a value of 10. Because plate rheology structure is tied to the thermal structure, plate thickness, as defined by rheology, may also vary between overriding and subducting plate in these cases (e.g., thin versus thick plates in Figure 2c).

Subduction Parameters

Results will be discussed primarily in terms of parameters which govern subduction morphology, plate structure (subducting and overriding plates) and subduction rate. Subduction morphology is to be discussed in terms of the ratio of retrograde to longitudinal slab motion (R_θ), as defined in Figure 3b. Figures 1 and 2c illustrate the two plate ages, or thermal boundary layer thicknesses, modeled in these experiments. Values of Ra_δ=70,000 and 500,000 produce initial TBL thicknesses of 70 and 45 km, representing old (thick) and young (thin) plates, respectively. Here TBL thickness is defined as the depth at which the fluid's potential temperature reaches 90% of the maximum value (or T=1). The majority of experiments reported here are for E=30, or a thick rheological plate. A value of E=30 corresponds to an activation energy of 500 kJ/mol, which is considered a reasonable value for the upper mantle. Additional experiments have been conducted with progressively thinner, weaker plates, for a given thermal structure, by using values of E=15 and 8 (Table 1) in the viscosity law.

With regard to subduction rate and morphology, results are to be presented with regards to two loosely defined sets of experimental conditions. In the first set, a "mixed" mode of slab forcing is modeled whereby slabs are both driven with an applied velocity and as a result of negative buoyancy forces. A common feature of this set of experiments (cases 1-24 in Table 1) is that subduction morphology remains essentially invariant (e.g., 45° dip angles, R_θ=0) in order to focus attention on how subduction rate and plate structure influence thermal evolution of the slab and mantle wedge. The magnitude of the applied subduction rate is represented as U_O, which is used in formulating a dimensionless (applied) Peclet number, $Pe=U_oD/\kappa$. The magnitude of buoyancy forcing is governed by Ra and B. In all cases with buoyant flow, Ra is set at 800,000 which corresponds to a slab-mantle density anomaly ($\alpha\Delta T$) of 2.5% and an ambient upper mantle viscosity of 1.5×10^{20} Pa s, assuming a total upper mantle potential temperature drop of 1250°C and a value for α of 2×10^{-5}.

A second grouping of experiments for discussion (cases 25-44 in Table 1) consider a range in ratios of retrograde (or prograde) slab motion to longitudinal slab motion (R_θ). R_θ variability is produced in two ways. In a series of experiments with mixed slab forcing, a range in R_θ values is produced by

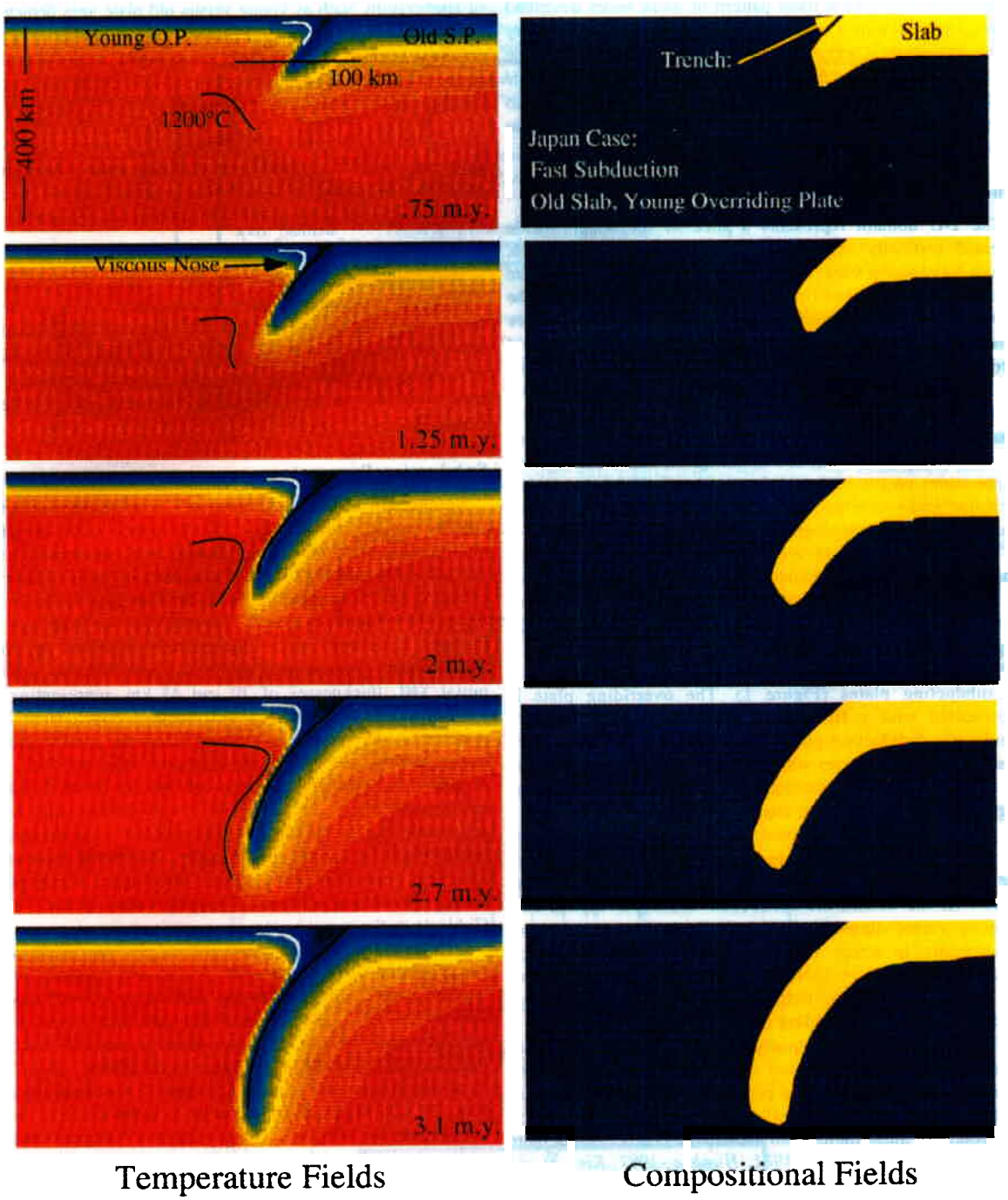

Plate 1. Composite showing the time evolution of subduction for a case (case 23 in Table 1) with an imposed Pe=3000 (or 10 cm/yr) convergence rate and Ra=800,000. Thermal fields are shown on the left, with red corresponding to warmer temperatures, and compositional fields on the right. Slab material is blue, background upper mantle is yellow. Slab material is a factor of 2 more viscous than ambient mantle at the same temperature (e.g., $\{\mu_o(C=1) / \mu_o(C=0)\} = 2$). Elapsed times are indicated in the temperature plots. This sequence shows the evolution of subduction from initiation until the slab reaches 400 km depth. The case is meant to represent Japan, where an old slab (Ra_δ=70,000; 70 km thick) sinks beneath a young plate (Ra_δ=500,000; 45 km thick). The dark line extending down from the trench, and the white line in the arc corner in the temperature fields mark the slab's material surface and the evolution of the viscous corner (or nose), respectively. The dark (1200°C) contour line highlights the evolution of the viscous boundary layer which blankets the slab's surface.

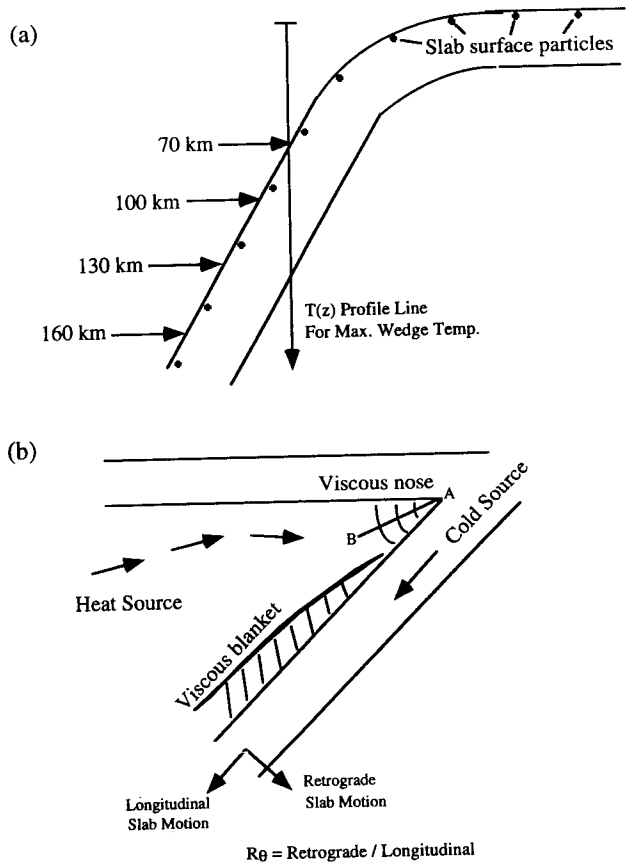

Figure 3. (a) Illustration of the two modes of temperature measurement along the slab's upper surface. In one case (Eulerian), the slab-wedge material interface is determined for a given depth level (70 km, 100 km, 130 km, and 160 km) and the temperatures of different slab surface particles occupying that spatial point are recorded. In another case (Lagrangian), temperatures of individual particles which make up the slab's material surface are recorded as they pass through the trench into the mantle. Included in this schematic is an example of a vertical line which pierces the slab-wedge interface at 70 km and along which temperatures are recorded. Similar profile lines are recorded through 160, 130, and 100 km slab surface depth horizons. (b) Schematic showing the balance between the slab, which represents a heat sink, and deeper return flow, which represents a heat source. Two predominant features which are produced by the temperature dependent viscosity are also represented including (1) a high-viscosity wedge corner and (2) the viscous blanket. R_θ is defined here as the ratio of retrograde to longitudinal slab motion.

varying the chemical density of the slab. This makes use of the models ability to tag slab fluid with particles because a chemical density (characterized by B) may be assigned to produce a range in R_θ values without otherwise altering initial thermal or rheological profiles within the subducting and overriding plates (cases 25-28 in Table 1). Experiments presented within this group also consider differences in slab-wedge thermal evolution arising from different modes of slab forcing (kinematic-buoyancy driven slabs). These cases are discussed in terms of parameters Pe, Ra, and B. However, because the most striking characteristic of this series of experiments (e.g., the dominant influence of kinematic versus dynamic slab forcing) is the range in retrograde (or prograde) to longitudinal slab subduction paths which are produced, these results are also discussed in terms of R_θ.

Model Outputs

One goal of these experiments is to understand how various subduction parameters influence the thermal evolution of the slab surface, specifically which conditions are most likely to result in melting of the slab sediments and oceanic crust. Moreover, we wish to determine how SSTs evolve from early to mature stages of subduction. To provide this information, SSTs are monitored in two distinct ways. One is an Eulerian record of the slab surface. At each time step the position of the chemical interface defining the slab's upper surface is determined for four depth horizons: 70 km, 100 km, 130 km, and 160 km, and the temperature is recorded (Figure 3a). This reference frame is that of an observer sitting at one of the specified depths and viewing the slab as it passes by. Because the slab surface is a material interface, the positions may be acquired regardless of how the slab evolves in time. The second measure is a Lagrangian record of temperature whereby temperature-depth paths are recorded for specific slab tracer particles as they move through the subduction zone (Figure 3a). Temperatures are recorded for particles distributed along the slab surface and at 2 km and 4 km depth levels within the slab. Finally, in order to document thermal conditions within the wedge, temperature profiles are recorded for various stages of subduction along vertical lines which pierce the slab's surface at depths of 70 km, 100 km, 130 km, and 160 km (as depicted in Figure 3a).

Results

The discussion of results from these numerical experiments will focus on (1) the role of variable temperature dependent viscosity on slab-wedge dynamics, (2) factors influencing thermal evolution of the slab and the core of the mantle wedge for cases in which $R_\theta \approx 0$, and (3) how variations (+/-) in R_θ produced either by different modes of slab forcing or through imposed compositional density differences influence slab-wedge thermal conditions. For topics 1 and 2, results are presented from calculations which utilize the mixed mode of forcing described above in which $R_\theta \approx 0$. Discussion of the third subtopic includes comparisons between cases in which slabs are driven kinematically (e.g., no slab buoyancy), dynamically (e.g., no applied slab velocity), or in a mixed fashion. One defining characteristic of these experiments is that they exhibit significant variability in R_θ.

Role of Temperature Dependent Viscosity

The thermal evolution of the wedge is governed by the competition between cooling from the slab and the advection of warmer mantle into the wedge with the return flow (Figure 3b). An important addition to this basic balance in subduction zones is that viscosity increases rapidly with decreasing temperature according to (8). The temperature dependent viscosity influences the wedge's evolution in two important ways. Plate 1 shows the development of the slab-wedge system in terms of temperature and compositional fields for conditions which are similar to subduction beneath Japan. Here an old (>70 km thick) slab moves beneath a young (45 km) overriding plate (case 23 in Table 1). The convergence rate is Pe=3000, which scales to a dimensional value of U_o=10 cm/yr, which

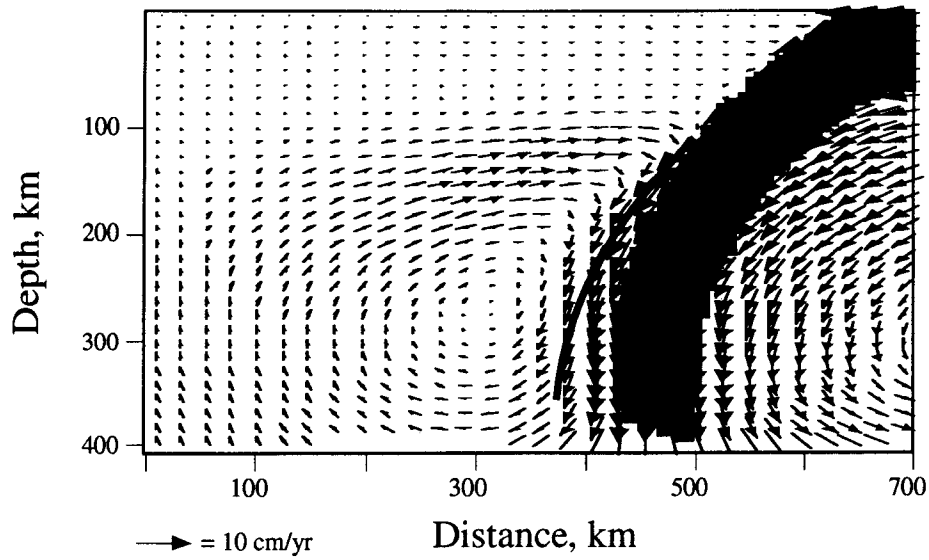

Figure 4. Velocity vectors plotted for the experiment shown in Plate 1 but after 3.5 Ma. The dark field is the slab, the dark line denotes the viscous boundary layer above the slab. Velocity vectors show the driven corner flow in the wedge and also show that the region of maximum shear occurs above the viscous boundary layer.

represents fast subduction. The compositional fields clearly illustrate the slab's descent. In this case the slab sinks with a 45° angle at a shallow depth, and because of negative slab buoyancy, slab dip angle increases at greater depths.

The thermal fields show two important features. We arbitrarily define the green-yellow contours (T=~0.7) to mark the viscous corner, or nose, of the subduction zone, shown schematically in Figure 3b. This contour band also roughly coincides with the maximum viscosity cutoff, such that below this temperature material viscosity falls off exponentially and above this value, viscosity is held fixed at μ=1000. This viscous corner region grows with time as the slab cools the mantle resulting in sluggish flow. A dark line in Plate 1 illustrates the deflection of the 0.95 potential temperature isotherm (or 1200°C assuming a ΔT=1250°C) from an initially horizontal orientation, up into the wedge corner as subduction develops. Hot wedge material is drawn upward toward the viscous corner. After roughly 3 m.y. the isotherm takes on a characteristic shape in which hotter material pinches in towards the slab interface at shallower levels [e.g., *Hsui et al.*, 1983] and bows outward from the slab surface at greater depths. Outside of this line, at these depths, viscosity is essentially invariant. However, inward of this line temperature drops and viscosity increases rapidly toward the slab. This line therefore marks the edge of the thermal boundary layer above the slab and a corresponding viscous boundary layer which blankets the slab's surface. Another dark line in the thermal fields extends downward from the trench marking the material interface between the slab and wedge. Note that the yellow temperature contour (or 1000°C potential temperature, assuming a ΔT=1250°C) does not pierce the slab's tip in any of these frames.

Figure 4 shows the velocity vectors for the case of a fast (U_o=10 cm/yr), old (70 km thick) slab beneath a young plate (45 km thick) as shown in Plate 1. The influence of the viscous blanket along the slab's upper surface on flow structure is that upper mantle material inside the viscosity boundary layer is moving at subducting plate speeds and is essentially part of the plate. Although this model does not include viscous shear heating, an important implication of this result is that the zone of maximum shear ($\partial u_s/\partial L$; where U_s is velocity in the downdip, or longitudinal, direction and L is distance normal to the slab surface) is deflected away from the slab surface. Maximum shear heat production in this case would not be at the slab interface but some 50 km or so out in the mantle wedge. Another important feature of this flow pattern is that because of the stagnant, high-viscosity corner, flow lines get squared off relative to a more typical constant viscosity corner flow pattern. In other words, there exists a 20 km thick region to the back arc (or left) side of the wedge corner where flow velocities are directed vertically downward toward the slab interface. It is important to note that this feature is influenced, in part, by the presence of the weak nodes which allow relative motion between the slab and overriding plate.

The growth of the viscous corner (or nose) out into the wedge versus the amount of slab material to have passed through the trench (or subduction length) is summarized in Figure 5a for cases with mixed forcing (R_θ≈0). The advancement of the nose into the wedge for a given increment of subduction length varies with Pe. For slowly subducting slabs, the nose is seen to grow more readily. In these slow cases a negative chemical buoyancy is applied to the slab (Table 1, cases 7-9). This is because as the nose grows beyond the limit of the weak nodes in these slow cases, the slab tends to underplate the overriding lithosphere. For higher subduction rates (Pe>800), the growth per unit subduction length is reduced and is approaching a steady value by 500 km. It is interesting to note that the growth trajectory passes through a minimum for Pe≈1500-2500 and then increases slightly for an even faster, Pe=5000, subduction rate. The pattern of decreased nose growth with Pe is attributed to the enhancement of return flow in the wedge with increasing Pe. The slight reversal of this trend for Pe=5000 is likely due to a perturbation of the balance which develops between slab cooling of the mantle wedge corner and heating/erosion by the mantle return flow. In other words, this superfast subduction sufficiently enhances the flux of cool slab

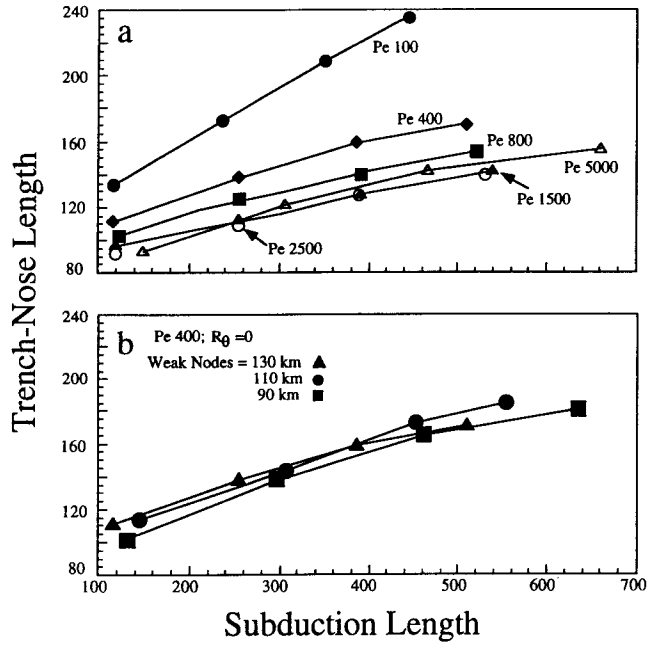

Figure 5. (a) Plot of distance along the line A-B, as shown in Figure 3b, to the dimensionless 0.65 isotherm versus length of slab to have subducted through the trench for cases with mixed slab forcing, R_θ=0 and thick plates (Table 1, cases 7-14). The growth of the viscous nose (per unit subduction length) decreases with increasing Pe. (b) Similar set of plots but for cases with fixed Pe (Table 1, cases 8, 30, and 38) showing that growth of the viscous nose is not reduced as the depth of weak nodes is reduced, provided that a 45° dip is maintained between cases (R_θ=0).

material past the wedge corner to give a small boost to the growth rate of the viscous nose. Reducing the depth extent of the weak nodes (Table 1, cases 29-39) does not significantly alter the growth rate profile for this feature, providing the dip angle remains at 45° (Figure 5b). The dominant effect of reducing the depth of weak nodes is to greatly enhance the amount of underplating which occurs between the subducting and overriding plates.

Slab Surface Temperature

Numerical experiments are used to provide a quantitative measure of variability in slab surface temperature (SST) and to discern which subduction parameters most strongly influence both SST and maximum temperatures in the mantle wedge beneath the volcanic front. In order to first focus attention on SST and wedge thermal evolution as a function of plate thermal structure and subduction rate, comparisons are made for cases with mixed forcing and a roughly constant, 45° dip angle (e.g., $R_\theta \approx 0$; cases 1-24 in Table 1). Principal variables in this comparison are listed in Table 1 and include subduction rate (Pe) and the plate's thermal structure characterized by Ra_δ.

Results from experiments with fixed E=30, $R_\theta \approx 0$ and similar subducting and overriding plate ages show that temperatures along the slab's upper surface during the early stages of subduction are controlled by both slab velocity and plate age. Figure 6 compares temperature and compositional fields for cases with different plate speeds and ages at similar stages of subduction (e.g., similar subduction lengths). Both SSTs and wedge temperatures are the lowest in the case of an old, thick plate because the return flow of asthenospheric material is limited in the wedge corner. Alternatively, with younger plates, a more vigorous return flow extends well into the wedge corner (Figure 6a versus Figure 6c) and both SSTs and wedge temperatures are higher.

SSTs are plotted at four depth levels over time to quantify the thermal evolution of the slab surface for different subduction rates and plate ages (Figure 7). Each curve shows the same basic evolutionary shape in that maximum temperatures are achieved early on, essentially when the slab tip pierces the specific depth horizon. SST then gradually decays with time and, in most cases, approaches a steady value. These plots show an expected trend in that temperature, at any given time, increases with depth along the slab-mantle interface. Plots also show that maximum temperatures are recorded in cases with slow subduction of a young plate beneath a young plate. Temperatures at each depth horizon systematically decrease as subduction rate increases (Figure 7b) and plate age increases (Figure 7c), which is in agreement with *Peacock* [1991]. A more detailed comparison of maximum recorded SST versus Pe for both old and young plates is given in Figure 8. For young plates, an approximate 30% reduction in maximum SST is noted over a range in subduction rates of Pe=100-5000 (0.3-16 cm/yr). While temperatures are uniformly lower for cases of old plates (Figure 8b), the variation with Pe is also reduced to roughly 20% over a similar Pe range.

In order to use these results to predict melting conditions within arcs, it is necessary to convert dimensionless potential temperatures to dimensional potential temperature and then to actual temperature values. To accomplish the first step, we assume two values for upper mantle potential temperature drop (ΔT). This value is essentially the deep, ambient mantle potential temperature (T_m), assuming T=0 at the surface. A value of T_m=1250°C is consistent with current estimates and a higher, T_m=1400°C, value corresponds to warmer conditions, such as is suggested for the Archean. To then convert to actual temperature, we assume an adiabatic gradient of 0.5°C/km. Both Figures 7 and 8 provide three distinct temperature-depth horizons above which melting of sediments is likely to occur. These are calculated based on a melting point of 900°C, which assumes that sediments roughly follow the solidus of wet basalt (J. Holloway, personal communication, 1995) at these pressures. The horizons (I and II) calculated for 160 km depth are for the two estimates of T_m. Figure 7a shows that temperatures are most likely to exceed the melting point of the sediments in the depth range of 130-160 km in young subduction zones, where plate rates are slow (<3-4 cm/yr). This result is consistent with models developed to explain petrologic evidence suggesting slab melting in cases of subduction of young, thin plates, such as in the Cascades [*Drummond and Defant*, 1990].

Increasing subduction rate reduces both the amplitude of the early SST pulse and the later stage temperatures relative to the slower cases (Figure 7b), particularly at shallow depth levels. Interestingly, late stage temperatures at greater (160 km) depths are similar for the two subduction rates. The similarity in temperatures at greater depths is attributed to a more pronounced pinch zone (or region of maximum heat flux into the slab) which develops at greater depths in the fast cases. SSTs are even lower, both in short- and long-term records, for cases with similar subduction rates but thicker/older plates (Figure 7c). Results suggest that in mature subduction zones, when flow and thermal fields are nearly steady state, SSTs are

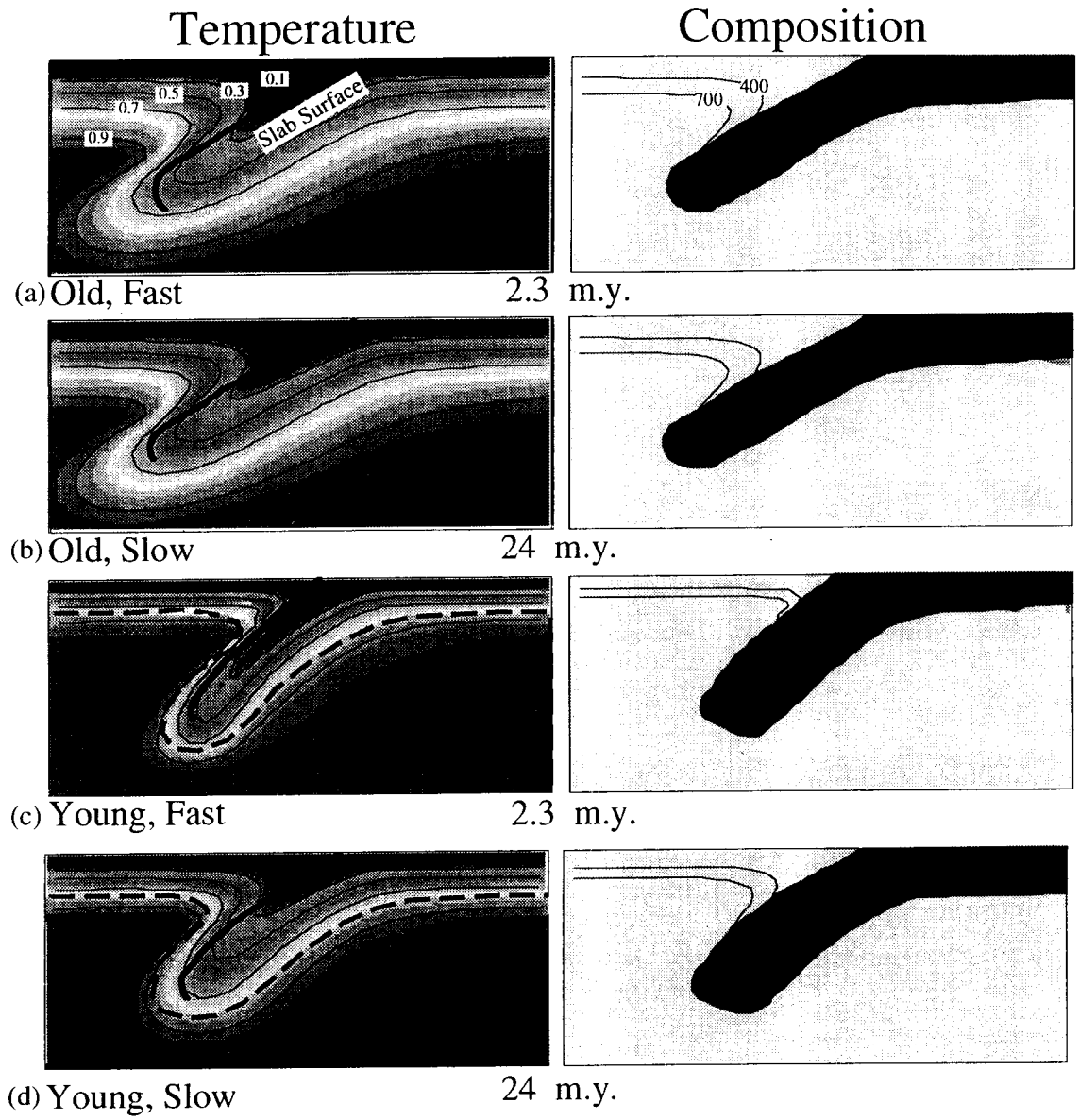

Figure 6. Upper mantle temperature and composition plots from four mixed cases at similar stages of evolution, or subduction length. In each case the subducting and overriding plates have the same initial structure, Ra is set at 800,000 and slab-mantle viscosity contrast is $\mu_o(C=1) / \mu_o(C=0) = 2$. The four cases are (a) fast (Pe=3000; 10 cm/yr) subduction with old, thick (70 km) plates, (b) slow (Pe=400, 1.3 cm/yr) subduction with old plates, (c) fast subduction with young, thin (45 km) plates, and (d) slow subduction with young plates (13, 8, 5 and 2 in Table 1). The thin dark lines in the temperature fields are dimensionless (potential) temperature contours. The thick dark lines and the dashed lines are the slab's surface and the μ=5 viscosity contour, respectively. The contour lines overlain in the compositional fields are mantle potential temperatures, calculated assuming T_m=1400°C (corresponding to T=1). Warmer slab temperatures are achieved with slower subduction rates. Higher wedge temperatures are recorded with faster subduction and thin overriding plates.

consistently below the dry solidus regardless of subduction parameters considered here. This latter result supports the model for magma genesis via fluxing of the mantle wedge with water from the subducted sediments over slab melting models.

The relationship between SST and plate rate and age is also apparent in the Lagrangian view of slab temperature evolution. Figure 9 shows temperature-depth paths of specific slab surface particles for a range in these subduction parameters. The two cases (Figures 9a and 9b) reflect choices for T_m of 1250°C and 1400°C. In addition, a distinction is made between early and late stage results in that T-z paths are given for particles initially positioned at the nose of the subducting plate (e.g., just at the trench) to record the initial transient versus 500 km back from the trench. By the time the latter particle has reached the trench the system is mature and approaching a steady state. These plots also show that chances of melting the slab surface (sediments or crust) are highest early on and fall off as the subduction zone matures. Moreover, SSTs are clearly highest for cases with slow, young plates. Only in the early stages of the young, slow case does SST pierce the wet basaltic

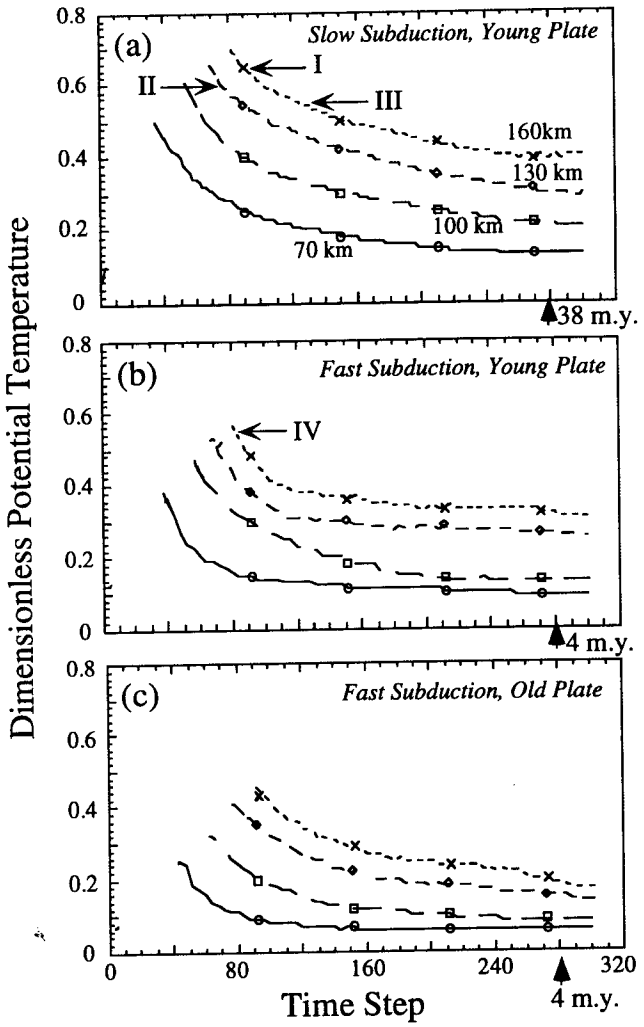

Figure 7. Plots of dimensionless potential temperature along the slab surface at four depth levels, as denoted in Figure 7a versus time. The primary variables are subduction rate (slow (1.3 cm/yr) versus fast (10 cm/yr)) and plate age (young (45 km) versus old (70 km)) and are listed for each plot. Temperatures are highest in each case as the slab first passes the given depth level and then steadily drop off thereafter. Temperatures are also highest in the case of slow subduction with thin plates. Estimates of melting horizons (e.g., temperature-depth position above which sediment melting should occur) are also shown. These are calculated using 900°C for a melting point, 0.5°C/km adiabatic gradient and one of two values for T_m including I, melting point at 160 km using T_m=1250°C; II, melting at 130 km for T_m=1400°C; III and IV, melting at 160 km for T_m=1400°C. For lower ambient mantle potential temperatures melting of sediments is only predicted early on for cases of slow subduction of young plates.

solidus. Given the higher T_m value (Figure 9b), the SST for the young, slow plate also approaches the wet peridotite solidus at depths >200 km. An important feature of these plots is that at later stages the slab surface remains extremely cool and well below melting conditions, regardless of plate rate or age.

Maximum Wedge Temperature

While the focus of this work is to determine which factors control the thermal evolution of the slab-wedge system, an important model output, with regards to arc melting models, is the maximum temperature a melt sees in traveling from the source region to the surface. The chemical character of island arc magmas is related to the thermal conditions within the mantle wedge through the temperature maximum, which modulates the mafic signature of the melt fluid. In order to quantify variability in maximum wedge temperature, thermal profiles are recorded along vertical lines which pierce the slab surface at depths of 100 km, 130 km and 160 km (as in Figure 3a). Figure 10a shows temperature profiles for end-member cases of fast (Pe=2000) and slow (Pe=400) subduction beneath a thin plate (Table 1, case 4 versus case 2). The plots highlight the fact that fluid (or melt) parcels traveling vertically from the slab will first go up in temperature and then down in temperature. Also, the slower plates produce cooler wedge temperatures but higher SSTs.

The relationship between maximum wedge temperature and Pe is summarized in Figures 10b and c for both old and young plates (Table 1, cases 1-14). Values are determined from late stage, or mature, temperature fields in each experiment. For both old and young plates, wedge temperatures generally increase with subduction rate. Results show, however, the age of the overriding plate has a strong influence on wedge thermal evolution. Maximum wedge temperatures produced at similar stages of subduction (e.g., subduction lengths) are roughly 25% greater for thin versus thick plate cases. Moreover, the pattern of increasing wedge temperature with Pe shows the strongest variation at lower Pe, between slow and intermediate subduction rates. At higher Pe this trend is seen to flatten as material with potential temperatures of T_m effectively penetrates into the wedge. This nonlinear trend is more

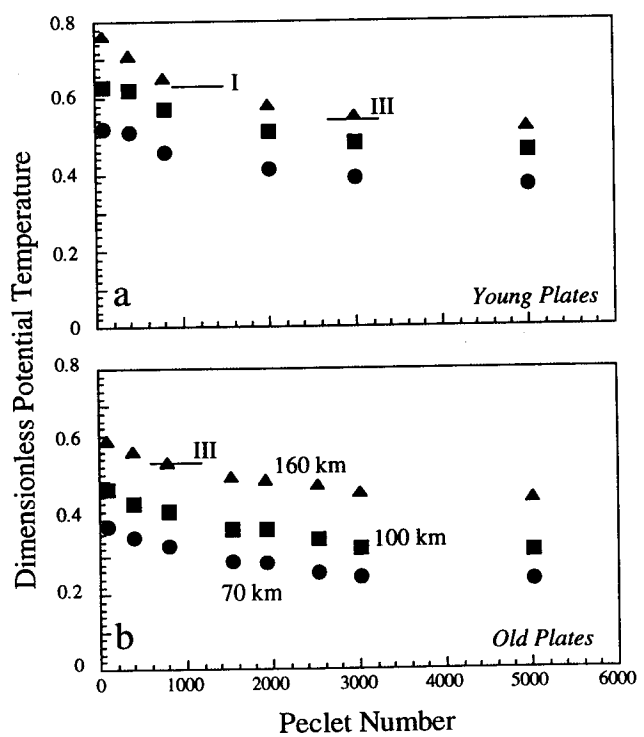

Figure 8. Plots of maximum slab surface dimensionless (potential) temperatures versus Pe at various depth horizons. Estimated melting points as determined in Figure 7 are also included for 160 km depth. Maximum SSTs (a) occur in cases of young plates and (b) show a larger range in values versus Pe for younger plates than with older plates.

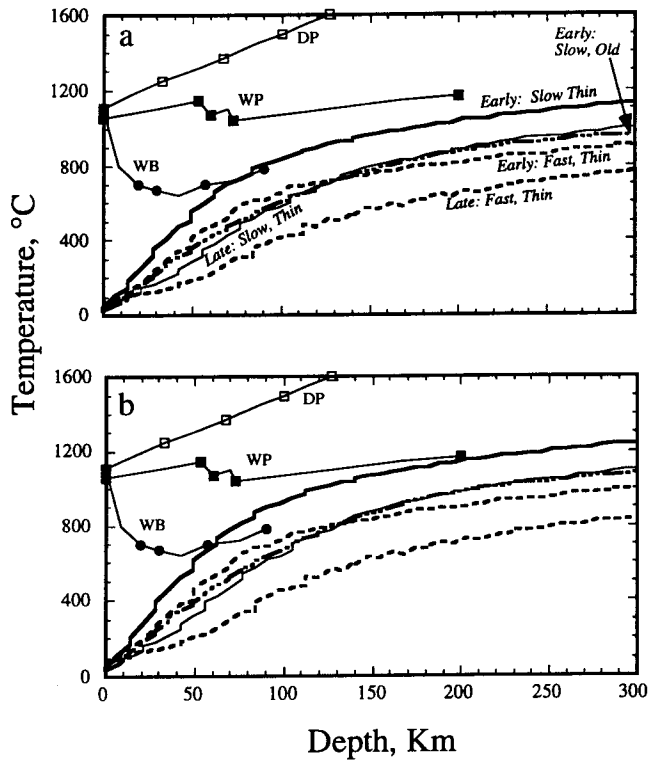

Figure 9. Temperature versus depth plots for specific slab surface particles covering a similar range in subduction parameters as in Figure 7. Temperatures represent actual values and are calculated using 0.5°C/km adiabatic gradient and either (a) T_m=1250°C or (b) T_m=1400°C. Plots labeled "early" represent thermal evolution of particles located within 10 km of the slab's leading edge. Plots labeled "late" are temperatures of particles initially located ≈ 500 km from the trench and so sample a more evolved wedge-slab system. The primary comparison is between early and late stage profiles for thin plates and for fast (Pe=3000) and slow (Pe=400) subduction rates. Maximum temperatures are recorded earlier and with slower plates. Also shown is the case for early subduction of an old, slow plate. For comparison, estimates of the wet (WP) and dry (DP) peridotite solidus [*Takahashi*, 1990] are given and the wet basaltic solidus [*Holloway and Burnham*, 1972; J. Holloway, personal communication, 1995].

accentuated with a young overriding plate, where material at T_m penetrates the wedge corner at lower subduction rates (from ≈3 cm/yr).

Finally, all cases presented to this point have considered the same plate rheological structure, for a given plate thermal profile (fixed E). Additional experiments have been run for a range in E values (Table 1). Decreasing E essentially produces a weaker plate. The primary result of varying E is summarized in the thermal-compositional fields in Plate 2. The thermal and rheological thickness of the lithosphere is progressively thinned in Plate 2a-2c (Table 1, cases 13, 15, and 16) and as a result subduction morphology evolves from a tabular slab sinking at 45° with R_θ≈0 to a slab sinking with R_θ>0 in which dip angle increases progressively with depth to produce a concave downward slab profile. The influence on the thermal fields are similar to the effect of reducing the thermal age of both overriding and subducting plates, as discussed above. Both SST (Table 1) and maximum wedge temperature increase as a more vigorous return flow is recorded within the wedge. This is evident in the pinch zone which has developed in Plate 2c.

Age of the Subducting Versus Overriding Plate

Up to this point, we have not distinguished between the influence of the overriding plate relative to the subducting plate. Additional experiments model SSTs and wedge temperatures for cases in which the subducting and overriding plates have different thicknesses or ages, as shown

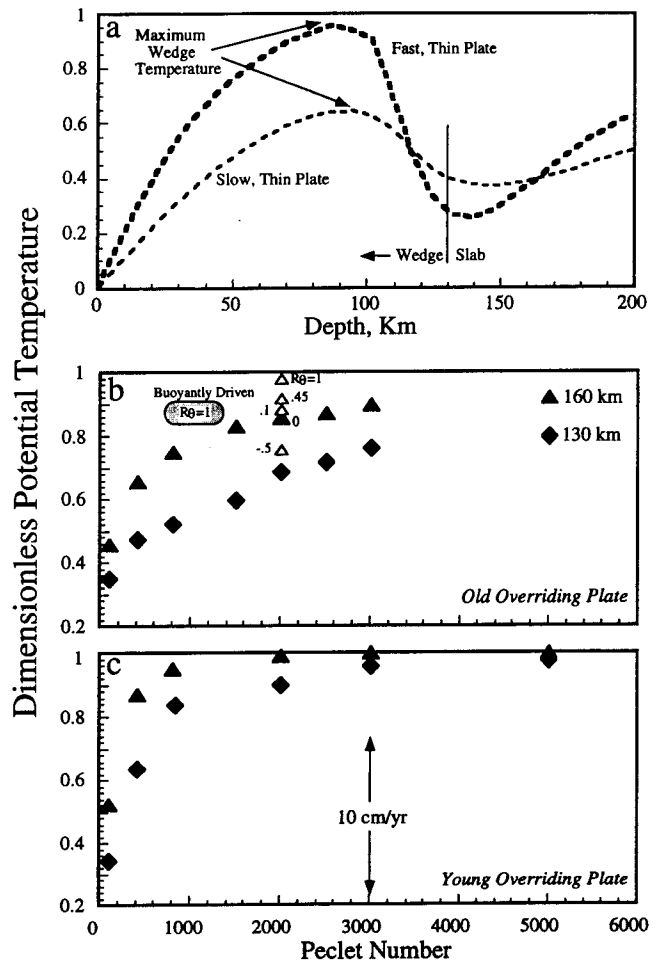

Figure 10. (a) Profiles of dimensionless potential temperature versus depth from mixed forcing cases (cases 2 and 4 in Table 1) highlighting conditions within the wedge for similar aged plates but different subduction rates. The profile is taken along a vertical line which pierces the slab's material surface (indicated on plot) at 130 km depth. Faster plates produce higher wedge temperatures but a lower SST. (b) Maximum wedge temperatures recorded for late stage (>500 km of subduction) thermal fields plotted as a function of Pe for cases with old overriding plates (Table 1, cases 7-14). Values are given for profiles piercing the slab surface at 130 km and 160 km depths. In these cases with mixed forcing the dip angles are all ≈45°, so the distance for each profile from the trench is roughly the same as the depth given in the plot. Also shown are values for mixed forcing and Pe=2000 but with varying R_θ (Table 1, cases 25-28) and a buoyantly-driven case (44 in Table 1). (c) Similar plot as in Figure 10b but for a young overriding plate (Table 1, cases 1-6). Conditions of rapid subduction beneath thin plates are optimal for achieving maximum wedge temperatures.

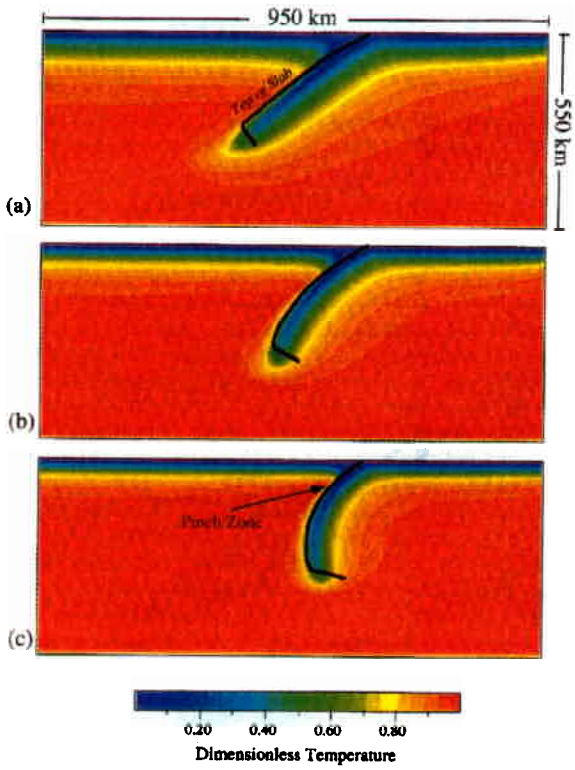

Plate 2. A comparison of temperature contours for cases highlighting the influence on slab morphology of thinning the plates, both thermally (larger R_δ) and viscously (smaller E). Each case utilizes mixed slab forcing, with Pe=3000. (a) A thick, strong plate (R_δ=75, 000 and E=30; case 13 in Table 1) subducts at 45°. Progressively weaker plates with (b) R_δ=200,000 and E=15 (Table 1, case 16) and (c) R_δ=500,000 and E=8 (Table 1, case 15) result in more pronounced wedge return flow into the wedge corner and higher R_θ ratios.

schematically in Figure 2c and described in (12). Experiments therefore consider old slabs subducting beneath young plates, as well as young plates beneath old plates. While temperatures might be expected to decrease with increasing age of the subducting plate, results indicate that age of the overriding plate can exert a strong influence on slab thermal evolution, to the point of offsetting this trend. Figure 11 shows patterns in Eulerian SST versus time for a number of these cases in which either subducting plate age is fixed and overriding plate age is varied, or vice versa. As with previous results, the slower plate rates produce warmer SSTs (e.g., Figures 11a versus Figure 11c). An interesting result is seen through a comparison of similar subduction rates. For instance, in comparing slow cases shown in Figures 11a and 11b, it is apparent that old subducting plates produce cooler SSTs, regardless of overriding plate thickness. However, for the fast cases shown in Figures 11c and 11d the influence of the overriding plate is more significant. Temperature profiles for old and young subducting plates are different when the overriding plate is thick. This is because wedge flow is restricted, and the uppermost corner of the wedge becomes heavily influenced by conduction from the cold slab. However, when the overriding plate is young and thin, the system may be more heavily modulated by the return flow within the wedge and its ability to erode the viscous corner such that essentially no difference between old and young subducting plates is observed. Faster plates increase the flux of cold material past the wedge, but this may be offset by a more vigorous flow of warm mantle with the return flow. These results indicate that at slow subduction rates the structure of the subducting plate is dominant, regardless of overriding plate structure, whereas in fast subduction zones, the structure of the overriding plate can strongly influence SST and, in some cases, be more important than the age of the subducting plate.

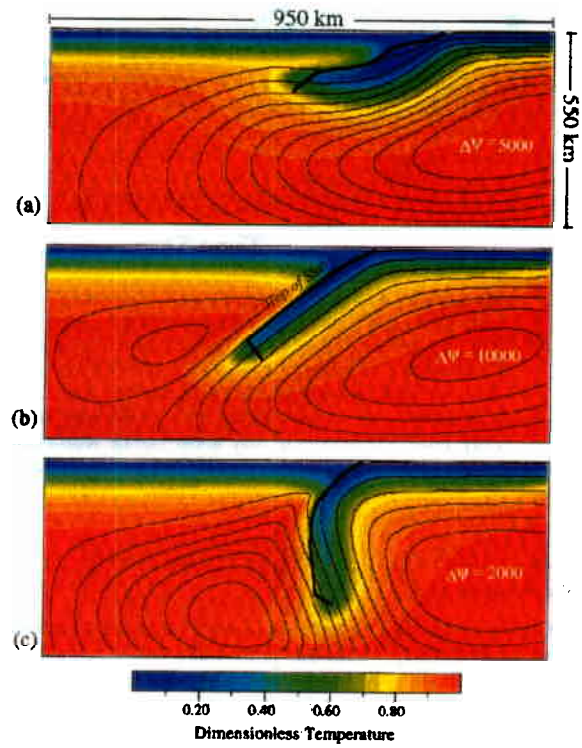

Plate 3. A comparison of temperature contours for cases with (a) purely kinematically driven slabs (Pe or $U_o \neq 0$; Ra=B=0), (b) mixed slab forcing cases (Pe or $U_o \neq 0$; Ra≠0, B=0), and (c) purely buoyantly-driven cases (U_o=0; Ra≠0; Rb≠0) to highlight the range in subduction morphologies produced (Table 1, cases 40, 13 and 44). Also shown are streamline patterns (dark lines). (a) The slab is viscously coupled with the overriding plate and subducts at a very low angle, essentially underplating the overriding plate. Wedge temperatures are low in these cases. (b) Mixed cases tend to produce a tabular slab, sinking at roughly 45°. The slab sinks with a primarily longitudinal component of slab motion (streamlines parallel to the slab's surface). Streamlines also show a relatively sluggish corner flow in the wedge. The low-angle subduction results in the freezing out of the arc corner, as discussed in Figures 3b, 4 and 5 and Plate 1, and a range in slab-wedge temperatures depending on subduction rate. (c) Cases with pure buoyantly driven slabs result in higher percentages of retrograde (streamlines crossing the slab surface) versus longitudinal subduction and steeper dip angles. The arc corner in this case is actually eroded with time.

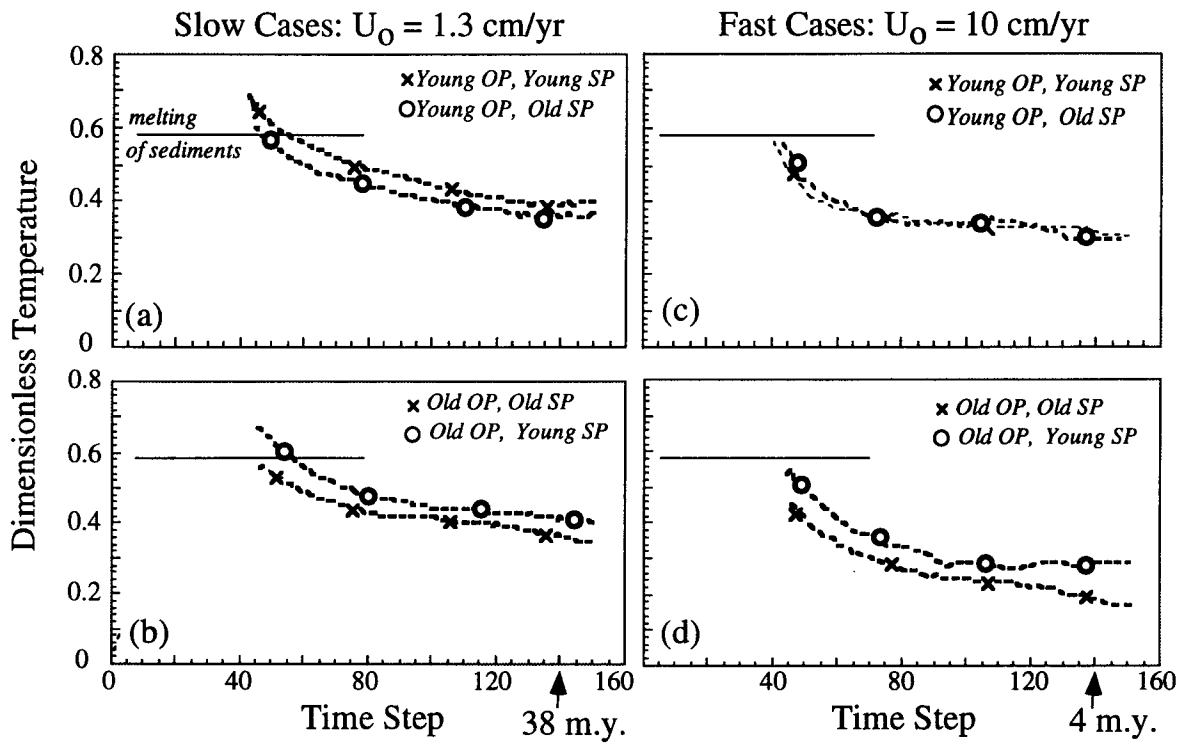

Figure 11. SST (at 160 km depth) versus time plots for cases with laterally variable plate thickness/age, as modeled with (10)-(12) and shown schematically in Figure 2c. An estimate of the sediment melting point is also shown (determined as in Figure 7 with T_m=1400°C). Comparisons are made between slow (Figures 11a and 11c) and fast (Figures 11b and 11d) subduction cases. Individual plots compare laterally variable plate cases (circles) with laterally uniform (crosses) plate cases to distinguish the influence of the overriding versus subducting plate in modulating SST. Generally older SPs produce cooler temperatures (e.g., Figures 11b and 11d), however, a thin OP may allow mantle return flow to modulate SST (e.g., Figure 11c) if subduction rate is large. Cases shown are numbered 21-24 in Table 1.

Mode of Slab Forcing: Driven Versus Purely Buoyant Slabs

One important difference between modeling a slab as a fixed, kinematic boundary within the domain and one which evolves freely, or dynamically, is the variation in slab morphology, both over time and with depth (e.g., shallow versus deep dip angles), and the related coupling between the slab and the flow of the upper mantle. The principal factor in controlling the evolution of slab morphology is the ratio of retrograde to longitudinal slab motion (Figure 3b) of individual parcels which make up the slab. This ratio is illustrated in Figure 3b and is defined by the ratio R_θ, (or retrograde/longitudinal motion vectors). For example, R_θ=0 is a measure of purely longitudinal motion, whereas values of R_θ=-1 and 1 represent equal parts of prograde and longitudinal and retrograde and longitudinal motion, respectively. In the majority of cases presented thus far, R_θ was intentionally kept close to zero, or dip angles of roughly 45°. This was to focus attention on thermal variability due only to factors such as subduction rate and plate age. Here results are presented for experiments which consider the influence of R_θ on the growth of the viscous nose, SST and wedge temperature. The variation in R_θ is produced in two ways. In experiments 25-28 (Table 1) slabs are driven with the mixed mode of forcing, and R_θ is varied by applying a chemical density contrast to the slab. In this way, the range in R_θ is produced without changing any other physical aspects of the system. A second method for producing a range in R_θ results from varying the mode of slab forcing between purely kinematic (e.g., imposed ridge push), mixed and purely buoyant (only slab pull) cases. Experiments 40-44 (Table 1) have been run with different modes of slab forcing, which may be characterized in terms of their behavior by R_θ, to show how kinematic versus dynamic forcing influences the evolution of the slab-wedge system.

Plate 3 shows temperature fields and streamlines for cases with old plates (70 km; no lateral variability) and fast subduction rates (10 cm/yr) but in which subduction is produced using these three different forcing modes. In Plate 3a, buoyancy is turned off, Ra=0, and the slab is seen to underplate the back-arc lithosphere. A high-temperature wedge is basically nonexistent between subducting and overriding plates. With a mixture of buoyancy and plate pushing (Table 1, case 13), subduction proceeds at a 45° dip angle (Plate 3b), or purely longitudinal motion, and SST and wedge temperature patterns are similar to those reported above. However, for buoyant only cases (Plate 3c) the slab sinks with both longitudinal and retrograde motion and rapidly assumes a nearly vertical morphology. The series of experiments in which slabs are driven with mixed forcing but in which B is varied to produce a range in R_θ sinking ratios (Table 1, cases 25-28) produce a range in subduction morphologies which are very similar to those cases shown in Plate 3. For example, values of B=-1.25, 0, and 3.75 in this series of experiments produce slab sinking profiles characterized by $R_\theta \approx$-0.5, 0, and

1 and patterns in slab-wedge evolution which generally correspond to those represented in Plates 3a, 3b and 3c, respectively.

Results from both sets of experiments in which R_θ varies substantially, from highly prograde to highly retrograde slab motion, show very different patterns in thermal evolution in the upper mantle as recorded through growth of the viscous nose, SSTs and wedge temperatures. For mixed cases in which Pe=2000 and B is varied to produce a range in R_θ, nose growth is most pronounced in association with prograde slab motion (R_θ <0) and decreases systematically with increasing R_θ (Figure 12a). Interestingly, maximum wedge temperature increases with R_θ in this series of experiments (Table 1, and Figure 10b) while maximum SST remains invariant between cases. The late stage SSTs are slightly larger in the R_θ <0 cases due to the increased path length to each of the specified depth horizons.

In these high R_θ cases with mixed slab forcing, shallow dip angles remain close to 45°, while deeper (>200 km) values approach 80-90°. The 45° shallow dip angle is constrained by a combination of the 45° dip of imposed velocity condition at the trench and the similar orientation of the weak nodes. When the slab is able to sink with R_θ >0 at shallow levels the viscous nose is seen to erode with increasing subduction length. Figure 12b shows this result for a case (case 32 in Table 1) where the depth extent of weak nodes are reduced and a large imposed B produces significant retrograde subduction. Here the nose evolution shows erosion is taking place as opposed to reduced weak node cases (Figure 5) where a value of $R_\theta \approx 0$ is maintained

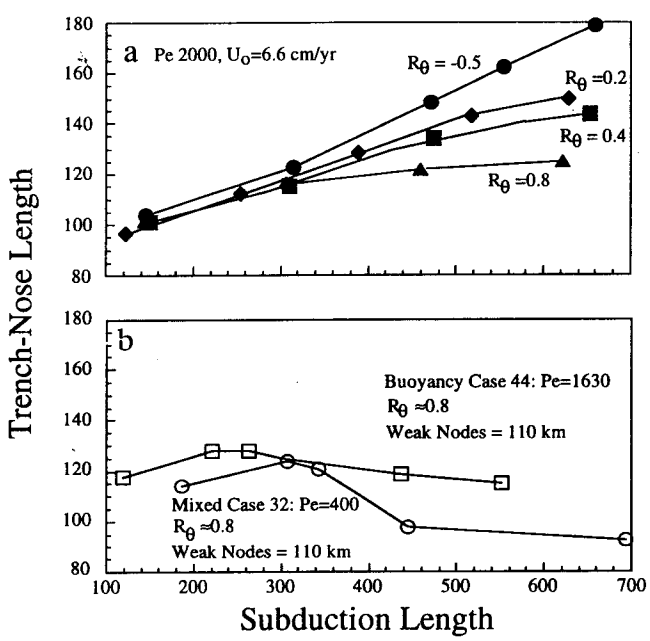

Figure 12. Similar plots of nose-trench distance versus subduction length as in Figure 5. (a) Values plotted for cases with mixed forcing and an applied Pe=2000 slab rate but varying R_θ values (cases 25-28 and 11 in Table 1). (b) Nose growth profiles are plotted for cases in which erosion of the viscous nose is optimal. These include experiments in which slabs are driven solely with negative buoyancy (Table 1, case 44 with large R_θ) and a mixed forcing case where both the depth extent of weak nodes is reduced and values of R_θ are large (Table 1, case 32). Both allow for retrograde slab motion at shallow levels in the subduction zone which serves to enhance the erosion of the viscous nose over R_θ=-1-0 cases.

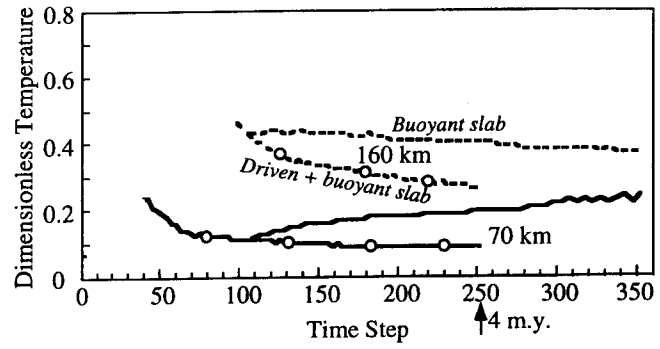

Figure 13. Comparison of SST (at a fixed depth) versus time plots for cases of subduction with mixed slab forcing (Table 1, case 13) and dynamic slabs driven purely by buoyancy (Table 1, case 44). The cases of dynamic slabs are begun with output from a mixed case with similar parameters after roughly 170 km of subduction. In both mixed and buoyant cases, the SP and OP are old/thick (70 km) and subduction rates are in the range of 5-10 cm/yr. The steeper dip angles and more substantial erosion of the arc corner in the purely buoyant cases lead to higher slab surface temperatures. In general, the pinch zone, where isotherms are compressed against the slab's surface, is broader and displaced upward along the slab-wedge interface in the buoyantly driven cases. Shallower SSTs (70-100 km) are seen to increase with time.

and the nose growth profile was only beginning to flatten after 500 km of subduction.

Driving slabs purely by buoyancy also has important effects on the thermal evolution of the slab and wedge. The larger dip angles and greater retrograde slab motion (R_θ >0) associated with buoyantly driven subduction produce vigorous return flow into the wedge. Perhaps more importantly, buoyantly driven slabs tend to sink with significant retrograde (R_θ >0) components of motion even at shallow (<100 km) depth levels. Common features of experiments with this style of subduction morphology are a well-developed pinch zone (or the region where the slab thermal boundary layer is thinnest) at the slab surface, just beneath the overriding plate, and significant erosion of the viscous nose with time (Figure 12b). This increased flow in the viscous corner is apparent in the streamline patterns in Plate 3c, which highlights the slab's ability to sink with a large component of retrograde motion at shallow levels. Finally, Figure 13 shows that SSTs for high R_θ, buoyantly driven cases decrease at greater depths, as with the mixed cases (Figure 7), but at a substantially lower rate. More striking is the fact that at shallow depths, SST actually increases with time. This reflects the erosion of the viscous corner and the migration of the pinch zone farther up the slab-wedge interface. Maximum wedge temperatures tend also to be higher in these cases than in experiments at comparable Pe but with $R_\theta \approx 0$ (Figure 10b).

Discussion

Results have been presented on the influence of various subduction parameters including subduction rate and plate ages, on SSTs and maximum wedge temperatures. In Figure 9 we summarized SST results versus published estimates for wet and dry peridotite solidus's and a wet basalt solidus. The plot clearly shows the dramatic difference in P-T paths experienced

by slab surface particles during early and late stages of subduction in that significantly higher temperatures are seen early on for slow subduction cases. In fact, melting of the sediments and possibly the oceanic crust is predicted under these conditions at relatively shallow levels. These results are consistent with petrologic models suggesting that melting of the slab might occur during the subduction of young, thin plates [*Drummond and Defant*, 1990]. It is interesting to note that under these same conditions, the slab surface geotherm grazes the wet peridotite solidus at greater (160-170 km) depths. Therefore any volatiles released from the slab at these depths would trigger immediate melting of the overlying peridotite wedge. During the early stages of subduction with faster plates, cooler geotherms are recorded such that without some other heat source (e.g., viscous heating) it is predicted that sediment melting will not occur. It is important to point out, however, that these experiments do not include viscous heat production and so represent minimum SST estimates.

After 500-600 km of subduction, all geotherms are well below conditions for melting which is consistent with seismic results from *Matsuzawa et al.* [1987] suggesting slab temperatures are sufficiently low to retard the basalt to eclogite transition. These results are also consistent with geochemically derived models for arc magmas [*Morris et al.*, 1990]. Models based on Be^{10}-B systematics suggest low temperatures are required to explain the presence of these elements in behind the front rocks.

The effect of variable viscosity, specifically, the evolution of the viscous blanket above the slab surface is also consistent with geochemical models which require the survival of sediments to great depths within subduction zones. Moreover, the high-viscosity wedge corner which freezes out to distances comparable to the position of the front rank of volcanoes is consistent with heat flow [*Hyndman*, 1988] and seismic attenuation patterns [*Umino and Hasegawa*, 1984]. Results show that in cases of fast subduction beneath young overriding plates, as in Japan, return flow into the wedge is enhanced. In particular, when slabs are driven buoyantly such that retrograde slab velocity is a significant proportion of longitudinal velocity ($R_\theta > 0$), wedge corner temperatures are largest (Figure 14). These results are consistent with tomography work of *Zhao and Hasegawa* [1993] which shows a hot tongue of mantle material protruding up into the mantle wedge, above the slab. Moreover, this type of vigorous return flow deep into the wedge might provide temperatures which are sufficient for melt generation within the middle portion of the wedge. Of course, these interpretations are largely dependent on volatile concentrations within the matrix as well as patterns in melt flowlines relative to the those of the matrix. Here we have only considered vertical paths through the mantle wedge.

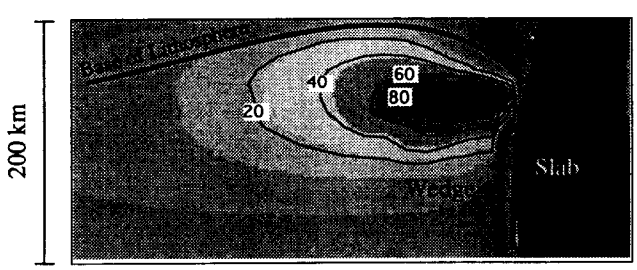

Figure 14. Close up contour plot of thermal conditions within the arc-wedge corner for the buoyantly driven case (case 44 in Table 1) in Plate 3c after 500 km of subduction. Contours represent excess (potential) temperature relative to overriding plate's initial thermal structure. A high-temperature pocket is noted above the slab's surface, in the vicinity of the arc-wedge corner.

Finally, these results predict that lavas between various subduction zones should follow specific patterns which are directly related to subduction parameters. For example, maximum slab temperatures are recorded for slow subduction beneath young plates. Since the ability for B to be retained with slab components decreases with higher slab temperatures, these results suggest, in a very simple way, that more B should be seen in cases with old, long running (steady), fast slabs subducting beneath old plates, such as Kermadac or New Britain. In contrast, results predict that less B should be seen in behind-the-front volcanoes for slow, young slabs subducting beneath young overriding plates, such as in the Antilles or Cascades.

Alternatively, results of these experiments indicate maximum wedge temperatures will be achieved in cases of fast subduction beneath thin plates. Higher wedge temperatures should be apparent at the surface in terms of higher eruptions temperatures and higher Mg contents. Concentrations of Ca and Na are expected to rise and fall, respectively, as wedge temperatures increase and lava compositions should become progressively more mafic, ranging from dacites to basalts to high-Al basalts. As one example, results would predict that wedge temperatures, and therefore factors such as Mg number, should systematically increase between the Antilles (a slow, shallow dipping slab), to the Aleutians or Kuriles (fast, shallow dipping slabs) to Vanuatu, Soloman and Marianas arcs (fast, steeply dipping slabs). *McCulloch and Gamble* [1991, Table 1] show higher Mg numbers, on average, for samples from Vanuatu than the Aleutians.

McCulloch and Gamble [1991] also use patterns in large ion lithophile (LIL) enrichment in island arc basalts as proxies for characterizing chemical fluxes into the wedge system from the slab versus mantle wedge return flow (e.g., enriched relative to mid-ocean ridge basalt (MORB) equal to greater slab component). Assuming the ability for a slab-derived fluid component to actually leave the slab and rise into the mantle wedge is loosely related to slab thermal conditions (higher slab temperatures equal to more fluid production and therefore higher slab fluid fluxes to the wedge), then old, fast slabs should show lower slab components. In a very simplistic way, this trend appears in their data [*McCulloch and Gamble*, 1991] by comparing Kermadac (old subducting plate) with Vanuatu (young subducting plate), which have similar subduction rates. Clearly, more detailed predictions and comparisons with arc chemical data sets require additional experiments which couple thermal and dynamical conditions within the slab-wedge system with models of melt production and chemical transport.

Conclusions

We investigate basic questions concerning how the slab and wedge evolve for a range in subduction parameters, including plate rate and age, and in cases when flow dynamics are considered using a two-dimensional, Cartesian model for subduction and dynamics of the upper mantle wedge. An important model feature is that the slab is defined chemically to enable us to track physical conditions along the material interface between the slab and wedge, without forcing this

interface to be a prescribed boundary within the domain. Basic conclusions of these experiments include the following:

1. Variable, temperature-dependent viscosity influences the evolution of the upper mantle wedge in two important ways. First, these experiments highlight the energy balance in the wedge between fluxes of cold and hot material associated with the sinking slab and the forced return flow from deep in the wedge. The forced flow works to erode the wedge corner, driving warmer isotherms deeper into the corner. The slab balances this by cooling the wedge corner and driving a thermal boundary layer out, away from the wedge corner. When the fluid viscosity varies strongly with temperature, a plug of highly viscous material develops and propagates with the cool boundary layer. This viscous nose causes the wedge corner to stagnate. The growth of the nose is seen to depend primarily on Pe for $R_\theta \approx 0$ cases but also increases (decreases) with increased levels of prograde (retrograde) slab motion. A second important outcome of the variable viscosity experiments is that they show the evolution of a viscous blanket above the slab through the adherence of upper mantle material onto the slab surface. This causes the zone of maximum velocity shear, as measured along a line drawn normal to the slab surface, to be deflected outward, away from the slab. If shear heating is important in subduction zones, this result implies that the zone of maximum shear heat production is not at the slab-wedge interface, where the sediments presumably reside, but at some distance out in the upper mantle. Further experiments which include viscous heating within the mantle wedge (along the lines of *Kincaid and Silver* [1996]) are currently being done to determine how this influences the growth of the viscous blanket.

2. The thermal evolution of the slab surface and therefore the subducted sediments is strongly influenced by the subduction rate, the age of the subducting plate, and factors controlling the flux of hot material into the wedge to oppose the cooling effects of the slab. Two important factors are the age/thickness of the overriding plate and the ratio of retrograde to longitudinal slab motion over time (e.g., slab dip angle). For a fixed dip angle ($R_\theta=0$), rapid subduction beneath a thicker overriding plate cools the wedge the most and results in the coolest SSTs. Maximum SSTs are recorded in slow subduction zones, where both the subducting and overriding plates are young and thin. In cases where subduction proceeds at relatively low velocity (<3cm/yr) beneath young, 40 km thick lithosphere the surface of the slab, in the vicinity of the leading edge, undergoes maximum heating. In the early stages of subduction, temperatures reach 800-900°C at 70 km depth, which should be sufficient to trigger melting of the sediments. Thicker overriding plates essentially choke off the deeper return flow allowing the cool boundary layer driven by the slab to advance into the wedge. An interesting result is that maximum slab temperatures occur early after subduction initiation and gradually decay with time. It should be noted, however, that this result is based on an assumption that the mantle into which the slab initially plunges has a laterally uniform temperature distribution. In mature subduction zones, when flow and thermal fields are nearly steady state, SSTs are consistently below the dry solidus which supports the model for magma genesis via fluxing of the mantle wedge with water from the subducted sediments over slab melting models.

In contrast to the slab, maximum wedge temperatures for $R_\theta=0$ cases are achieved with faster subduction rates, which drive stronger return flow up into the wedge corner. Wedge temperatures are largely invariant to slab age but are enhanced with thinner overriding plates.

3. A number of important deviations to (1) evolution of the viscous nose, (2) SST, and (3) maximum wedge temperature are noted for cases with $R_\theta \neq 0$. These differences are recorded whether the retrograde (or prograde) motion is produced by a variation in the mode of slab forcing or simply through an applied chemical density contrast. For example, the morphology and evolution of the slab-wedge system vary significantly depending on the mode of slab forcing in that for pure ridge push cases, there is essentially no wedge as the slab drags along beneath the overriding plate ($R_\theta<0$). Wedge temperatures are significantly lower for prograde subduction. For purely slab pull cases (buoyant only), the slab sinks with longitudinal and retrograde motion such that dip angle increases with both time and depth ($R_\theta>0$). The larger dip angles allow for more vigorous wedge return flow and, therefore, both higher maximum wedge temperatures and higher SSTs than the mixed, longitudinal only ($R_\theta \approx 0$) cases. Moreover, the highly viscous wedge corner is eroded as the ratio of retrograde to down dip subduction velocity increases and a more pronounced "pinch" zone develops in the slab's thermal boundary layer at shallow (100 km) levels.

Acknowledgments. We thank U. Christensen, S. King, and one anonymous reviewer for their suggestions on improving this manuscript. This work was supported by NSF award EAR-9219796.

References

Abers, G. A., Three-dimensional inversion of regional *P* and *S* arrival times in the East Aleutians and sources of subduction zone gravity highs, *J. Geophys. Res.*, *99*, 4395-4412, 1994.

Anderson, R.N., S.E. Delong, and W.M. Schwarz, Thermal model for subduction with dehydration in the downgoing slab, *J. Geol.*, *86*, 731-739, 1978.

Barr, T.D., and F. A. Dahlen, Brittle frictional mountain building, 2, Thermal structure and the heat budget, *J. Geophys. Res.*, *94*, 3923-3947, 1989.

Brooks, A., A Petrov-Galerkin finite-element formulation for convection dominated flows. Ph.D. thesis, Calif. Inst. of Technol., Pasadena, 1981.

Chase, C. G, Extension behind island arcs and motions relative to hot spots, *J. Geophys. Res.*, 83, 5385-5387, 1978.

Christensen, U., Mixing by time-dependent convection, *Earth Planet. Sci. Lett.*, *95*, 382-394, 1989.

Christensen, U., An Eulerian technique for thermomechanical modeling of lithospheric extension, *J. Geophys. Res.*, *97*, 2015-2036, 1992.

Christensen, U., and D.A. Yuen, The interaction of a subducting lithospheric slab with a chemical of phase boundary, *J. Geophys. Res.*, *89*, 4389-4402, 1984.

Davies, G.F., Mantle convection under simulated plates: Effects of heating modes, ridge and trench migration, and implications for the core-mantle boundary, bathymetry, the geoid and Benioff zones, *Geophys. J. R. Astron Soc.*, *84*, 153-183, 1986.

Davies, J.H., and M. J. Bickle, A physical model for the volume and composition of melt produced by hydrous fluxing above subduction zones, *Philos. Trans. Roy. Soc. London, Ser. A*, *335*, 355-364, 1991.

Davies, J.H., and D.J. Stevenson, Physical model of source region of subduction zone volcanics, *J. Geophys. Res.*, *97*, 2037-2070, 1992.

Drummond, M.S., and M.J. Defant, A model for trondhjemite-tonalite-dacite genesis and crustal growth via slab melting: Archean to modern comparisons, *J. Geophys. Res.*, *95*, 21,503-21,521, 1990.

Dumitru, T.A., Effects of subduction parameters on geothermal gradients in forearcs, with an application to franciscan subduction in California, *J. Geophys. Res.96*, 621-641, 1991.

Edwards, C.M.H., J.D. Morris, and M.F. Thirlwall, Separating mantle from slab signatures in arc lavas using B/Be and radiogenic isotope systematics, *Nature*, *362*, 530-533, 1993.

Furukawa, F., Magmatic processes under arcs and formation of the volcanic front, *J. Geophys. Res.*, *98*, 8309-8319, 1993a.

Furukawa, F., Depth of the decoupling plate interface and thermal structure under arcs, *J. Geophys. Res.*, *98*, 20,005-20,013, 1993b.

Furukawa, Y., and S. Uyeda, Thermal state under the Tohoku arc with consideration of crustal heat generation, *Tectonophysics*, *164*, 175-187, 1989.

Garfunkel, Z., C. A. Anderson, and G. Schubert, Mantle circulation and the lateral migration of subducted slabs, *J. Geophys. Res.*, *91*, 7205-7223, 1986.

Gill, J. B., J. D. Morris, and R. W. Johnson, Timescale for producing the geochemical signature of island arc magmas: U-Th-Po and Be-B systematics in recent Papua New Guinea lavas, *Geochim. Cosmochim. Acta.*, *57*, 4269-4283, 1993.

Gurnis, M. and B. Hager, Controls on the structure of subducted slabs, *Nature*, *335*, 317-321, 1988.

Hager, B. H., and R. J. O'Connell, Subduction zone dip angles and flow driven by plate motion, *Tectonophysics*, *50*, 111-133, 1978.

Harper, J. F., Asthenosphere flow and plate motions, *Geophys. J. R. Astron. Soc.*, *55*, 87-110, 1978.

Helffrich, G., and S. Stein, Study of the structure of the slab-mantle interface using reflected and converted seismic waves, *Geophys. J. Int.*, *115*, 14-40, 1993.

Holloway, J. R., and C. W. Burnham, Melting relations of basalt with equilibrium water pressure less than total pressure, *J. Petrol.*, *13*, 1-29, 1972.

Hsui, A.T., B.D. Marsh, and M.N. Toksoz, On melting of the subducted oceanic crust: Effects of subduction induced mantle flow, *Tectonophysics*, *99*, 207-220, 1983.

Hughes, T. J. R., *The Finite Element Method*, 631pp., Prentice-Hall, Englewood Cliffs, N.J., 1987.

Hyndman, R. D., Dipping seismic reflectors, electrically conductive zones and trapped water in the crust over a subducting plate, *J. Geophys. Res.93*, 13391-13405, 1988.

Jacoby, W.R., and H. Schmeling, On the effects of the lithosphere on mantle convection and evolution, *Phys. Earth Planet. Int.*, 29, 305-319, 1982.

Jackson, I., M. S. Paterson, and J. D. Fitz Gerald, Seismic wave dispersion and attenuation in Aheim dunite: An experimental study, *Geophys. J. Int.*, *108*, 517-534, 1992.

Jurdy, D. M., and M. Stefanick, Flow models for back-arc spreading, *Tectonophysics*, *99*, 191-200, 1983.

Kincaid, C., Laboratory and numerical experiments on subduction and subduction-related processes, Ph.D. thesis, Johns Hopkins Univ., Baltimore, Md., 1990.

Kincaid, C., and P. Olson, An experimental study of subduction and slab migration, *J. Geophys. Res.92*, 13,832-13,840, 1987.

Kincaid, C., and P. Silver, The role of viscous dissipation in the orogenic process, *Earth Planet. Sci. Lett.*, *142*, 271-288, 1996.

Kincaid, C., I.S.Sacks, and M. Spiegelman, The thermal, chemical and dynamical evolution of the upper mantle in subduction zones, *Eos Trans. AGU*, 75 (44), Fall Meet Suppl., 641, 1994.

Kincaid, C., J.-G., Schilling, and C. Gable, The dynamics of off-axis plume-ridge interaction in the uppermost mantle, *Earth Planet. Sci. Lett.*, *137*, 29-43, 1996.

King, S.D., and B. H. Hager, The relationship between plate velocity and trench viscosity in Newtonian and power-law subduction calculations, *Geophys. Res. Lett.*,*17*, 2409-2412, 1990.

King, S.D., and J. J. Ita, Subduction and volatile recycling in Earth's mantle, in *Volatiles in the Earth and Solar System*, edited by K. Farley, *AIP Conf. Proc. 341*, 1-12, 1995.

King, S.D., A. Raefsky, and B. H. Hager, ConMan: Vectorizing a finite element code for incompressible, two-dimensional convection in the Earth's mantle, *Phys. Earth Planet. Inter.*, *59*, 195-207, 1990.

Marsh, B.D., Island arc development: some observations, experiments and speculations, *J. Geol.*, *87*, 687-713, 1979.

Matsuzawa, T., N. Umino, A. Hasegawa, and A. Takagi, Upper mantle velocity structure estimated from *PS*-converted wave beneath the northeastern Japan arc, *Geophys. J. R. Astron. Soc.*, *86*, 767-787, 1986.

Matsuzawa, T., N. Umino, A. Hasegawa, and A. Takagi, Estimation of the thickness of a low-velocity layer at the surface of the descending oceanic plate beneath the northeastern Japan arc by using synthesized *PS*-wave, *Tohoku Geophys. J.*, *31*, 19-28, 1987.

McCulloch, M. T., and J. A. Gamble, Geochemical and geodynamical constraints on subduction zone magmatism, *Earth Planet. Sci. Lett.*, *102*, 358-374, 1991.

Molnar, P., and P. England, Temperatures, heat flux, and frictional stress near major thrust faults, *J. Geophys. Res.*, *95*, 4833-4856, 1990.

Molnar, P., W.-P. Chen, and E. Padovani, Calculated temperatures in overthrust terrains and possible combinations of heat sources responsible for the Tertiary granites in the greater Himalaya, *J. Geophys. Res.*, *88*, 6415-6429, 1983.

Morris, J. D., W. P. Leeman, and F. Tera, The subducted component in island arc lavas: Constraints from Be isotopes and B-Be systematics, *Nature*, *344*, 31-36, 1990.

Ogawa, M., G. Schubert, and A. Zebib, Numerical simulations of three-dimensional thermal convection in a fluid with strongly temperature-dependent viscosity, *J. Fluid Mech.*, *233*, 299-328, 1991.

Ohtaki, T., and S. Kaneshima, Continuous high velocity aseismic zone beneath the Izu-Bonin arc, *Geophys. Res. Lett.*, *21*, 1-4, 1994.

Olson, P., and C. Kincaid, Experiments on the interaction of thermal convection and compositional layering at the base of the mantle, *J. Geophys. Res.*, *96*, 4347-4354, 1991.

Parmentier, E. M., and J. E. Oliver, A study of shallow mantle flow due to the accretion and subduction of lithospheric plate, *Geophys. J. R. Astron. Soc.*, *57*, 1-22, 1979.

Peacock, S. M., Numerical simulation of subduction zone pressure-temperature-time paths: Constraints on fluid production and arc magnetism, *Philos. Trans. R. Soc. London, Ser. A*, *335*, 341-343, 1991.

Peacock, S. M., Blueschist-facies metamorphism, shear heating, and *P-T-t* paths in subduction shear zones, *J. Geophys. Res.*, *97*, 17,693-17707, 1992.

Peacock, S., T. Rushmer, and A. Thompson, Partial melting of subducting oceanic crust, *Earth Planet. Sci. Lett..*, *121*, 227-224, 1994.

Reagan, M.K., J.D. Morris, E. A. Herrstrom, and M. T. Murrell, Uranium series and beryllium isotope evidence for an extended history of subduction modification of the mantle below Nicaragua, *Geochim. Cosmochim. Acta*, *58*, 4199-4212, 1994.

Richards, M., and G.E. Davies, On the separation of relatively buoyant components from subducted lithosphere, *Geophys. Res. Lett.*, *16*, 831-834, 1989.

Sacks, I.S., Anomalous island arc asthenosphere and continental growth, *Year Book Carnegie Inst. Washington*, *74*, 256-266, 1975.

Sacks, I.S., and C. Kincaid, On slab melting in subduction zones, *Eos Trans. AGU*, 71(43), 1714, 1990.

Sato, H., and I.S. Sacks, Magma generation in the upper mantle inferred from seismic measurements in peridotite at high pressure and temperature, in *Magma Tansport and Storage*, edited by M.P. Ryan, John Wiley, New York, pp. 277-292, 1990.

Schmeling, H., Compressible convection with constant and variable viscosity: The effect on slab formation, geoid, and topography, *J. Geophys. Res.*, *94*, 12,463-12,481, 1989.

Schmeling, S., and W. R. Jacoby, On modeling the lithosphere in mantle convection with non-linear rheology, *J. Geophys. 50*, 89-100, 1981.

Shemenda, A. I., Horizontal lithosphere compression and subduction: Constraints provided by physical modeling, *J. Geophys. Res.*, *97*, 11,097-11,116, 1992.

Shemenda, A. I., Subduction of the lithosphere and back arc dynamics: Insights from physical modeling, *J. Geophys. Res.*, *98*, 16,167-16,185, 1993.

Spiegelman M., and D. McKenzie, Simple 2-D models for melt extraction at mid-ocean ridges and island arcs, *Earth Planet. Sci. Lett.*, *83*, 137-152, 1987.

Spiegelman, M., C. Kincaid, and I.S. Sacks, Arcs still suck: Not-so-simple models for melt and fluid transport in subduction zones, *Eos Trans. AGU*, (44)*75*, Fall Meet. Suppl., 641, 1994.

Staudigel, H., and S. D. King, Ultrafast subduction: The key to slab recycling efficiency and mantle differentiation?, *Earth Planet. Sci. Lett.*, *109*, 517-530, 1992.

Takahashi, E., Speculations on the Archean mantle: Missing link between komatite and depleted garnet peridotite, *J. Geophys. Res.*, *95*, 15,941-15,954, 1990.

Tao, W. C., and R. J. O'Connell, Ablative subduction: A two-sided alternative to the conventional subduction model, *J. Geophys. Res.*, *97*, 8877-8904, 1992.

Tatsumi, Y., Migration of fluid phases and genesis of basalt magmas in subduction zones, *J. Geophys. Res.*, *94*, 4697-4707, 1989.

Toksoz, N., and P. Bird, Formation and evolution of marginal basins and continental plateaus, in *Island Arcs, Deep Sea Trenches, and Back-Arc Basins, Maurice Ewing Ser.*, vol. 1, edited by M. Talwani and W. C. Pitman III, pp. 379-393, AGU, Washington, D.C., 1977.

Toksoz, N., J.W. Minear, and B.R. Julian, Temperature field and geophysical effects of a down-going slab, *J. Geophys. Res.*, *76*, 1113-1138, 1971.

Tovish, A., G. Schubert, and B. P. Luyendyk, Mantle flow pressure and

the angle of subduction: Non-Newtonian corner flows, *J. Geophys. Res.*, *83*, 5892-5898, 1978.

Travis, B., C.J. Anderson, J. Baumgardner, C.W. Gable, B.H. Hager, R.J. O'Connell, P. Olson, A. Raefsky, and G. Schubert, A benchmark comparison of numerical methods for infinite Prandtl number convection in a two-dimensional geometry, *Geophys. Astrophys. Fluid Dyn.*, *55*, 137-160, 1991.

Umino, N., and A. Hasegawa, Three-dimensional Q_S structure in the northeastern Japan arc, *J. Seismol. Soc. Jpn.*, *37*, 217-228, 1984.

van den Berg, A. P., D. A. Yuen, and P. E. van Keken, Effects of depth variations in creep laws on the formation of plates in mantle dynamics, *Geophys. Res. Lett.*, *18*, 2197-2200, 1991.

Van der Hilst, R., R. Engdahl, W. Spakman, and G. Nolet, Tomographic imaging of subducted lithosphere below northwest Pacific island arcs, *Nature*, *353*, 37-43, 1991.

Van der Hilst, R., R. Engdahl, and W. Spakman, Tomographic inversion of *P* and *pP* data for aspherical mantle structure below the northwest Pacific region, *Geophys. J. Int.*, *115*, 264-302, 1993.

Zhao, D., and A. Hasegawa, *P* wave tomographic imaging of the crust and upper mantle beneath the Japan Islands, *J. Geophys. Res.*, *98*, 4333-4353, 1993.

Zhong, S., and M. Gurnis, Role of plates and temperature-dependent viscosity in phase change dynamics, *J. Geophys. Res.*, *99*, 15,903-15,917, 1994.

Zhong, S., and M. Gurnis, Viscous flow model of a subduction zone with a faulted lithosphere: Long and short wavelength topography, gravity and geoid, *Geophys. Res. Lett.*, *19*, 1891-1894, 1992.

C. Kincaid, Graduate School of Oceanography, University of Rhode Island, Narragansett, RI 02882-1197. (e-mail: kincaid@lighthouse.gso.uri.edu).

I.S. Sacks, Carnegie Institution of Washington, Department of Terrestrial Magnetism, 5241 Broad Branch Road, N.W., Washington, DC 20015.

(Received June 6, 1996; revised November 7, 1996; accepted November 12, 1996.)